The ALMA Survey of 70 mu m Dark High-mass Clumps in Early Stages (ASHES). VII. Chemistry of Embedded Dense Cores

(article starts on next page)

The ALMA Survey of 70 μm Dark High-mass Clumps in Early Stages (ASHES). VII. Chemistry of Embedded Dense Cores

Shanghuo Li[1,2] , Patricio Sanhueza[3,4] , Xing Lu[5] , Chang Won Lee[1,6] , Qizhou Zhang[7] , Stefano Bovino[8] , Giovanni Sabatini[9] , Tie Liu[5] , Kee-Tae Kim[1,6] , Kaho Morii[10] , Daniel Tafoya[11] , Ken'ichi Tatematsu[3] , Takeshi Sakai[12] , Junzhi Wang[5] , Fei Li[13] , Andrea Silva[3] , Natsuko Izumi[14] , and David Allingham[15]

[1] Korea Astronomy and Space Science Institute, 776 Daedeokdae-ro, Yuseong-gu, Daejeon 34055, Republic of Korea; shanghuo.li@gmail.com
[2] Max Planck Institute for Astronomy, Königstuhl 17, D-69117 Heidelberg, Germany
[3] National Astronomical Observatory of Japan, National Institutes of Natural Sciences, 2-21-1 Osawa, Mitaka, Tokyo 181-8588, Japan
[4] Department of Astronomical Science, SOKENDAI (The Graduate University for Advanced Studies), 2-21-1 Osawa, Mitaka, Tokyo 181-8588, Japan
[5] Shanghai Astronomical Observatory, Chinese Academy of Sciences, 80 Nandan Road, Shanghai 200030, People's Republic of China
[6] University of Science and Technology, 217 Gajeong-ro, Yuseong-gu, Daejeon 34113, Republic of Korea
[7] Center for Astrophysics | Harvard & Smithsonian, 60 Garden Street, Cambridge, MA 02138, USA
[8] Departamento de Astronomía, Facultad Ciencias Físicas y Matemáticas, Universidad de Concepción, Av. Esteban Iturra s/n Barrio Universitario, Casilla 160, Concepción, Chile
[9] INAF—Istituto di Radioastronomia—Italian node of the ALMA Regional Centre (It-ARC), Via Gobetti 101, I-40129 Bologna, Italy
[10] Department of Astronomy, Graduate School of Science, The University of Tokyo, 2-21-1, Osawa, Mitaka, Tokyo 181-0015, Japan
[11] Department of Space, Earth and Environment, Chalmers University of Technology, Onsala Space Observatory, 439 92 Onsala, Sweden
[12] Graduate School of Informatics and Engineering, The University of Electro-Communications, Chofu, Tokyo 182-8585, Japan
[13] School of Astronomy and Space Science, Nanjing University, 163 Xianlin Avenue, Nanjing 210023, People's Republic of China
[14] Academia Sinica Institute of Astronomy and Astrophysics, 11F of AS/NTU Astronomy-Mathematics Building, No.1, Section 4, Roosevelt Road, Taipei 10617, Taiwan
[15] School of Mathematical and Physical Sciences, University of Newcastle, University Drive, Callaghan, NSW 2308, Australia

Abstract

We present a study of the chemistry toward 294 dense cores in 12 molecular clumps, using data obtained from the ALMA Survey of 70 μm dark High-mass clumps in Early Stages. We identified 97 protostellar cores and 197 prestellar core candidates, based on the detection of outflows and molecular transitions of high upper-energy levels ($E_u/k > 45$ K). The detection rate of the N_2D^+ emission toward the protostellar cores is 38%, which is higher than 9% for the prestellar cores, indicating that N_2D^+ does not exclusively trace prestellar cores. The detection rates of the DCO^+ emission are 35% for the prestellar cores and 49% for the protostellar cores, which are higher than those for N_2D^+, implying that DCO^+ appears more frequently than N_2D^+ in both prestellar and protostellar cores. Both the N_2D^+ and DCO^+ abundances appear to decrease from the prestellar to the protostellar stage. The DCN, C_2D, and ^{13}CS emission lines are rarely seen in the dense cores of early evolutionary phases. The detection rate of the H_2CO emission toward dense cores is 52%, three times higher than that for CH_3OH (17%). In addition, the H_2CO detection rate, abundance, line intensities, and line widths increase with the core evolutionary status, suggesting that the H_2CO line emission is sensitive to protostellar activity.

1. Introduction

The chemical compositions of planets are affected by the chemical makeups of the protoplanetary disks within which they form. The chemical contents of the prestellar and protostellar cores set the initial conditions in protoplanetary disks (Caselli & Ceccarelli 2012; Drozdovskaya et al. 2019; Jørgensen et al. 2020; Booth et al. 2021; Öberg & Bergin 2021). Molecular lines are a powerful tool for revealing the chemical and physical processes during star formation and core evolution, since different molecules can be associated with specific chemical and physical environments (Bergin & Tafalla 2007). Consequently, different molecular lines can be used to probe different gas environments, i.e., different physical

conditions. For instance, deuterated molecules (e.g., N_2D^+, DCO^+, H_2D^+, and NH_2D) can be used to trace cold and dense molecular clumps/cores associated with early evolutionary stages of star formation (e.g., prestellar cores; Caselli et al. 2002; Kong et al. 2017; Giannetti et al. 2019; Sabatini et al. 2020; Li et al. 2021; Redaelli et al. 2021; Sakai et al. 2022). On the other hand, high-density gas tracers could also suffer from depletion toward cold and dense regions (e.g., N_2H^+—Pagani et al. 2007; N_2D^+—Redaelli et al. 2019; NH_3—Pineda et al. 2022). A prestellar core would further evolve into a protostellar core, in which protostars launch molecular outflows and heat the surrounding material. These physical processes can cause molecules to be released from the grain surface to the gas phase, causing the enhancement of various molecules in the gas phase (van Dishoeck & Blake 1998; Herbst & van Dishoeck 2009). CO and SiO are frequently used to probe protostellar activities (e.g., Sanhueza et al. 2010, 2017; Li et al. 2019, 2020; Lu et al. 2021), i.e., molecular jets and outflows. Formaldehyde (H_2CO) and methanol (CH_3OH) are commonly seen in star-

forming regions, and their abundances can be significantly enhanced with respect to quiescent regions in the presence of protostellar activity (e.g., molecular outflows; Arce et al. 2008; Sakai et al. 2012; Sanhueza et al. 2013; Jørgensen et al. 2020; Morii et al. 2021; Tychoniec et al. 2021). In addition, both species play key roles in the formation of more complex organic molecules, such as amino acids and other prebiotic molecules (Bernstein et al. 2002; Muñoz Caro et al. 2002; Garrod et al. 2008; Guzmán et al. 2013), which might be transported to circumstellar disks and potential planetary systems (Drozdovskaya et al. 2019). Thus, a full understanding of the chemical properties of star-forming clouds is essential for improving our knowledge of the physical and chemical processes that take place during star formation.

Numerous observational investigations have aimed at understanding the chemistry of star-forming molecular clouds. For instance, single pointing observations of a sample of massive clumps using single-dish telescopes (e.g., infrared dark clouds, or IRDCs—Sanhueza et al. 2012; Vasyunina et al. 2014; IRDCs to hot cores—Gerner et al. 2014; Sabatini et al. 2021), single-dish mapping of a sample of massive clumps (e.g., IRDCs—Miettinen 2014; IRDCs to H II regions—Hoq et al. 2013), interferometer/single-dish observations toward several massive clumps (e.g., IRDCs—Feng et al. 2020; H II regions—Li et al. 2017), interferometer observations of a sample of H II regions (Qin et al. 2022), and case studies (e.g., Sanhueza et al. 2013; Immer et al. 2014; Liu et al. 2020; Peng et al. 2022). Thanks to these observational studies of chemistry toward different star formation regions, our understanding of chemistry has been significantly advanced; for instance, chemical abundances of molecular species vary significantly throughout the evolutionary sequence of star-forming regions.

Despite these advances, the chemical properties of prestellar and protostellar cores are still unclear, due to the lack of observations of a large sample of dense cores at early evolutionary stages. Here, we use Atacama Large Millimeter/submillimeter Array (ALMA) high-sensitivity and high–spatial resolution data to investigate the chemistry of a statistically significant sample ($N = 294$) of spatially resolved deeply embedded dense cores, which are still at extremely early evolutionary stages of star formation. The data were obtained by the ALMA Survey of 70 μm dark High-mass clumps in Early Stages (ASHES), first presented in Sanhueza et al. (2019; hereafter, Paper I). The molecular outflow content and the CO depletion fraction of the detected ASHES cores are presented in Li et al. (2020; hereafter, Paper II) and Sabatini et al. (2022), respectively. Case studies are presented in Tafoya et al. (2021), Morii et al. (2021), and Sakai et al. (2022).

Among the 294 dense cores revealed in the continuum emission, we have identified 197 prestellar core candidates (hereafter, prestellar cores) and 97 protostellar cores. The numbers of prestellar and protostellar cores have been updated, thus they are slightly different from the 210 prestellar and 84 protostellar cores reported in Paper I. A core is classified as "prestellar" (category 1) if it is not associated with molecular outflows and/or emission from any of the three lines CH$_3$OH $4_{2,2} - 3_{1,2}$ ($E_u/k = 45.46$ K), H$_2$CO $3_{2,2} - 2_{2,1}$ ($E_u/k = 68.09$ K), or H$_2$CO $3_{2,1} - 2_{2,0}$ ($E_u/k = 68.11$ K). A core is classified as an "outflow core" (category 2) if it is associated with outflows detected in the molecular line emission, but without the detection of any of the three aforementioned lines (Paper II). Details of the molecular outflows are presented in Paper II.

A core is classified as a "warm core" (category 3) if it is associated with emission from any of the three aforementioned lines, but without outflow detection. The "warm core" refers to an evolutionary stage prior to the "hot-core" phase. A core is classified as an "outflow + warm core" (category 4) if it is associated with emission from any of the three aforementioned lines, as well as with outflows. Overall, categories 2, 3, and 4 are considered as protostellar cores.

In this work, we study the chemistry of embedded dense cores in the extremely early evolutionary stages of high-mass star-forming regions, using high–angular resolution and high-sensitivity ALMA observations. With a statistically significant sample of dense cores, we will study the properties of deuterated molecules (N$_2$D$^+$, DCO$^+$, C$_2$D, and DCN) and dense gas tracers (C^{18}O, H$_2$CO, CH$_3$OH, and ^{13}CS). The paper is organized as follows. Section 2 describes the observations. The results and analysis are presented in Section 3. In Section 4, we discuss the results. A summary of the main conclusions is presented in Section 5.

2. Observations

Observations of 12 70 μm dark molecular clumps were performed with ALMA in Band 6 ($\sim$224 GHz; 1.34 mm), using the main 12 m array, the 7 m array, and the total power array (TP; Project ID: 2015.1.01539.S, PI: P. Sanhueza). The mosaic observations were carried out with the 12 m array and 7 m array, to cover a significant portion of the clumps, as defined by single-dish continuum images. The same correlator setup was applied for all sources. More details on the observations can be found in Papers I and II.

Data calibration was performed using the CASA software package, versions 4.5.3, 4.6, and 4.7, while the 12 m and 7 m array data sets were concatenated and imaged together using the CASA 5.4 `tclean` algorithm (McMullin et al. 2007). Data cubes for lines were produced using the `yclean` script, which automatically cleans each map channel with custom-made masks (Contreras et al. 2018). The imaging process uses two times the σ rms threshold. The continuum emission was obtained by averaging the line-free channels in visibility space. We used a multiscale clean for the continua and data cubes, with scale values of 0, 5, 15, and 25 times the image pixel size of 0″.2. Since some sources were observed with different configurations, a uv taper was used for such sources, in order to obtain a similar synthesized beam of $\sim$1″.2 for all sources. We adopted Briggs robust weightings of 0.5 and 2 for the visibilities of the continua and the lines in the imaging process, respectively. This achieved an averaged 1σ noise level of $\sim$0.1 mJy beam^{-1} for the continuum images. For the detected molecular lines (N$_2$D$^+$ $J = 3$–2, DCN $J = 3$–2, DCO$^+$ $J = 3$–2, C$_2$D $J = 3$–2, ^{13}CS $J = 5$–4, SiO $J = 5$–4, C^{18}O $J = 2$–1, CO $J = 2$–1, CH$_3$OH $4_{2,2} - 3_{1,2}$, and H$_2$CO $3_{0,3} - 2_{0,2}$, $3_{2,2} - 2_{2,1}$, and $3_{2,1} - 2_{2,0}$), the sensitivities are $\sim$9.5 mJy beam^{-1} per 0.17 km s^{-1} for the first six lines and $\sim$3.5 mJy beam^{-1} per 1.3 km s^{-1} for the last six lines (see Table 1). The 12 m and 7 m array line emissions were combined with the TP observations through the feathering technique. All images shown in this paper are prior to primary beam correction, while all measured fluxes are corrected for primary beam attenuation.

Table 1
Summary of Detected Lines and Their Parameters

Molecule	Transition	Frequency (GHz)	E_u/k (K)	$S_{ij}\mu^2$ D^2	n_{crit} (cm^{-3})	Q_{rot}	Rotational Constants (MHz)	Beam Size (″)	rms
DCO$^+$	$3-2$	216.112	20.74	45.624	1.84E+06	$0.58T_{ex} + 0.34$		1.5×1.0	9.5[a]
C$_2$D	$3-2$	216.373	20.77	2.541	8.18E+05	$3.47T_{ex} + 2.06$		1.6×1.0	9.5[a]
SiO	$5-4$	217.105	14.48	48.146	1.22E+06	$\frac{k_B T_{ex}}{h B_0} + \frac{1}{3}$	$B_0 = 21711.97$	1.6×1.0	9.5[a]
DCN	$3-2$	217.238	20.85	80.501	2.16E+07	$0.1T_{ex}^{3/2} + 50.51$		1.7×1.0	9.5[a]
p-H$_2$CO	$3_{0,3} - 2_{0,2}$	218.222	20.95	16.308	2.56E+06	$\frac{1}{3}\left(\frac{\pi k_B^3 T_{ex}^3}{h^3 A_0 B_0 C_0}\right)^{0.5}$	$A_0 = 281970.56$	1.5×1.0	3.5[b]
p-H$_2$CO	$3_{2,2} - 2_{2,1}$	218.475	68.09	9.062	2.96E+06		$B_0 = 38833.987$	1.5×1.0	3.5[b]
p-H$_2$CO	$3_{2,1} - 2_{2,0}$	218.76	68.11	9.062	3.36E+06		$C_0 = 34004.244$	1.5×1.0	3.5[b]
CH$_3$OH	$4_{2,2} - 3_{1,2}$	218.44	45.46	13.906	2.04E+07	$\frac{1}{2}\left(\frac{\pi k_B^3 T_{ex}^3}{h^3 A_0 B_0 C_0}\right)^{0.5}$	$A_0 = 127523.4$	1.5×1.0	3.5[b]
							$B_0 = 24690.2$		
							$C_0 = 23759.7$		
C^{18}O	$2-1$	219.56	15.81	0.024	9.33E+03	$\frac{k_B T_{ex}}{h B_0} + \frac{1}{3}$	$B_0 = 54891.42$	1.5×1.0	3.5[b]
^{13}CS	$5-4$	231.22	32.73	38.335	4.46E+06	$1.85T_{ex} - 3.32$		1.4×1.0	9.5[a]
N$_2$D$^+$	$3-2$	231.321	22.2	312.104	1.70E+06	$4.87T_{ex} + 2.81$		1.5×1.0	9.5[a]

Note. E_u/k and $S_{ij}\mu^2$ are obtained from the Cologne Database for Molecular Spectroscopy (https://cdms.astro.uni-koeln.de/cdms/portal/; Müller et al. 2005). The critical densities are estimated using the equation $n_{crit} = A_u/\gamma$, where Einstein A coefficients (A_u) and collisional rates (γ) at 20 K were obtained from the Leiden atomic and molecular database (Schöier et al. 2005). For N$_2$D$^+$, DCN, and C$_2$D, we use the same collision rates as for N$_2$H$^+$, HCN, and C$_2$H, respectively, since the lack of direct experimental constraints and the transitions between the deuterated and nondeuterated isotopologue do not differ significantly. The collision rate value of ^{13}CS is from its main isotopologue. The rotational constants (i.e., A_0, B_0, C_0) are retrieved from the splatalogue database for astronomical spectroscopy (https://splatalogue.online//). a: the unit is mJy beam^{-1} per 0.17 km s^{-1}. b: the unit is mJy beam^{-1} per 1.3 km s^{-1}.

3. Results and Analysis

At the moment, the ALMA TP antennas do not provide continuum emission observations. Therefore, our analysis of the continua and molecular lines is mostly focused on combined 12 m and 7 m images (hereafter, 12m7m), whereas the combined 12 m, 7 m, and TP images (hereafter, 12m7mTP) are used to assess the missing flux in images without TP data.

The astropy astrodendro package (Rosolowsky et al. 2008; Astropy Collaboration et al. 2013) was employed to identify the embedded dense cores for each clump (Paper I). A minimum value of 2.5σ, a step of 1.0σ, and a minimum number of pixels equal to those contained in half of each synthesized beam were used to extract the dense cores (i.e., the leaves, in the terminology of astrodendro). To eliminate spurious detections, we only considered cores with integrated flux densities $>3.5\sigma$ (see Section 4.2 in Paper I for more details of the identification of dense cores).

Figure 1 shows the velocity-integrated intensity (also known as 0th-moment) maps of N$_2$D$^+$, DCO$^+$, DCN, H$_2$CO $(3_{0,3} - 2_{0,2})$, CH$_3$OH, and C^{18}O for G014.492–00.139 (hereafter, G14.49), but excluding C$_2$D, ^{13}CS, CO, and SiO. The 0th-moment images of molecular lines for the remaining clumps are presented in Appendix A. Among the three H$_2$CO transitions, we focus on the H$_2$CO $(3_{0,3} - 2_{0,2})$ line, unless otherwise noted. H$_2$CO $(3_{0,3} - 2_{0,2})$ traces cold dense gas better than the other two transitions, $3_{2,2} - 2_{2,1}$ and $3_{2,1} - 2_{2,0}$, which preferentially trace warm dense gas. The C$_2$D and ^{13}CS lines are only detected in very limited regions toward 10 dense cores. The spatial distributions of the CO and SiO lines can be found in Paper II. Both the CO and C^{18}O lines show significant emission throughout the clumps, although there is a significant depletion in their emission toward some dense cores. Both N$_2$D$^+$ and DCO$^+$ lines are preferentially present around or toward the dense cores. CH$_3$OH and H$_2$CO emission lines are frequently found around outflows and dense cores. The majority of the DCN line emission appears toward the protostellar cores.

3.1. Detection Rates

In general, the emission from deuterated species is weak. For all the detected lines of interest, the spectra are averaged inside the dendrogram leaf (see Paper I) that defines each core, in order to increase the signal-to-noise ratio (S/N). We derive the line central velocity (v_{LSR}), the observed velocity dispersion ($\sigma_{obs} = $ FWHM$/2\sqrt{2 \ln 2}$), and peak intensity (I) from Gaussian fittings to the core-averaged spectrum for each line, except for N$_2$D$^+$, which is fitted with a hyperfine structure (hfs) model. The derived σ_{obs} is not corrected by the smearing effect, due to the channel width. To increase the S/N of the weak line emission, the core-averaged spectrum is spectrally smoothed over two native channels, prior to Gaussian/hfs fittings, if it shows marginal $\sim3\sigma$ confidence in the native spectral resolution. The best-fit parameters, which are used to compute the column densities of molecules (see Appendix C) and the following analyses, are summarized in Appendix A.

CO emission is detected in all the identified cores. C^{18}O is detected in 267 of the 294 cores, with a detection rate of 89%. H$_2$CO is the third most commonly detected line, which is detected in 156 of the 294 cores, with a detection rate of 52%. CH$_3$OH is detected in 51 of the 294 cores, leading to a detection rate of 17%. Among the detected deuterated species, DCO$^+$ is the most commonly detected line, with a detection rate of 39% (116/294). N$_2$D$^+$ is detected in 54 of the 294 cores, resulting in a detection rate of 18%. There are seven cores that are associated with the DCN line emission, with a detection rate of 2%. There is weak C$_2$D emission in three dense cores, with a detection rate of 1%. ^{13}CS is detected toward four dense cores, with a detection rate of 1%. Based on the core-averaged spectra, SiO emission is detected in 27 cores.
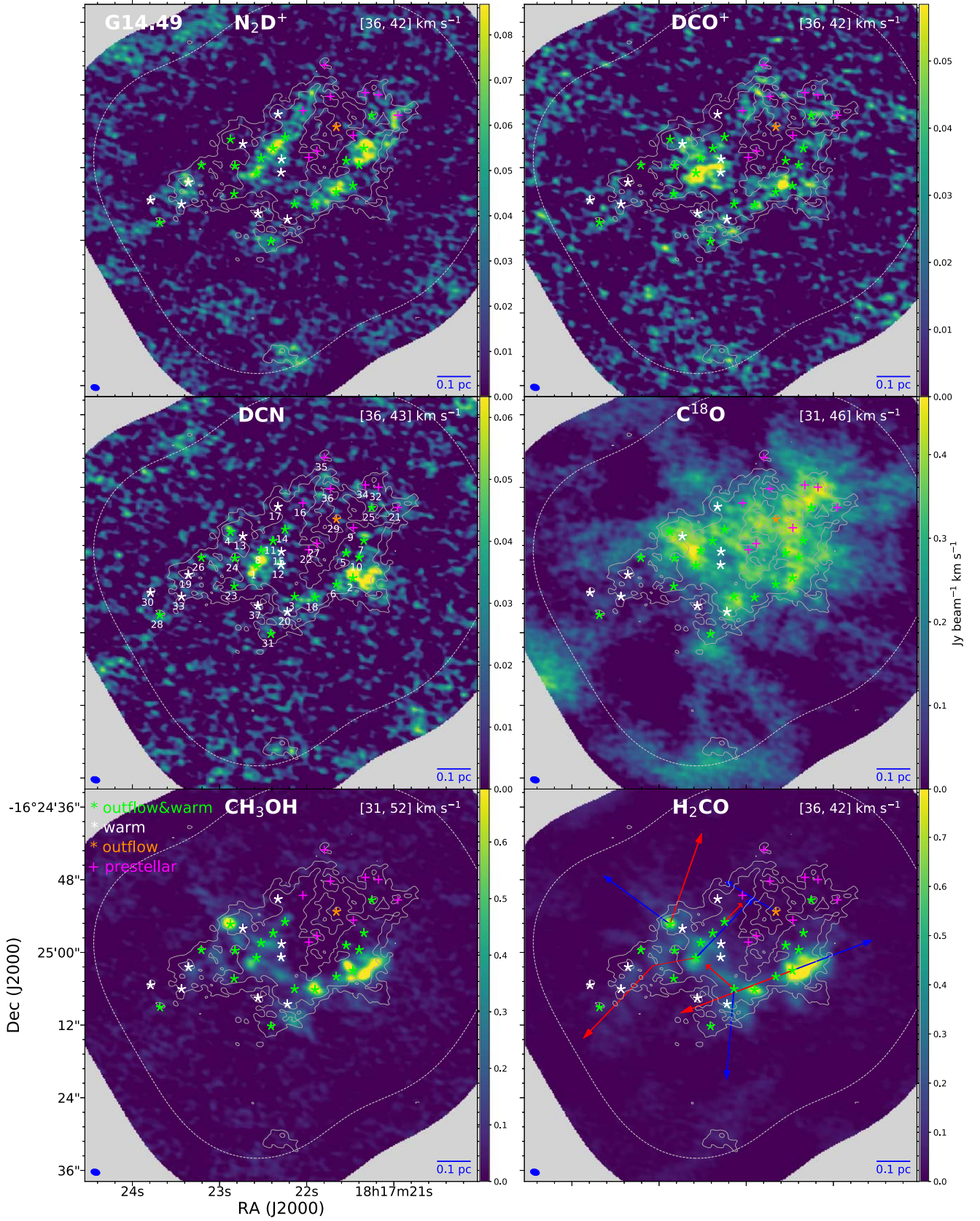
Figure 1. The velocity-integrated intensity maps of the N_2D^+, DCO^+, DCN, $C^{18}O$, CH_3OH, and H_2CO emission lines toward G14.49. The unit of the colorbar is Jy beam^{-1} km s^{-1}. The fuchsia pluses and yellow, white, and green asterisks indicate prestellar candidates (category 1), outflow cores (category 2), warm cores (category 3), and outflow + warm cores (category 4). The white dashed line shows 30% of the sensitivity level of the mosaic in the ALMA continuum image. The blue and red arrows in the bottom right panel indicate the directions of the blueshifted and redshifted CO outflow lobes (see Paper II), respectively. The gray contours in each panel show the 1.3 mm continuum emission. The contour levels are $(3, 6) \times \sigma$, with $\sigma = 0.115$ mJy beam^{-1}. The beam sizes of the line emissions and scale bars are shown in the lower left and right corners of each panel, respectively. The remaining sources are presented in Appendix A (see Figures 10–14).
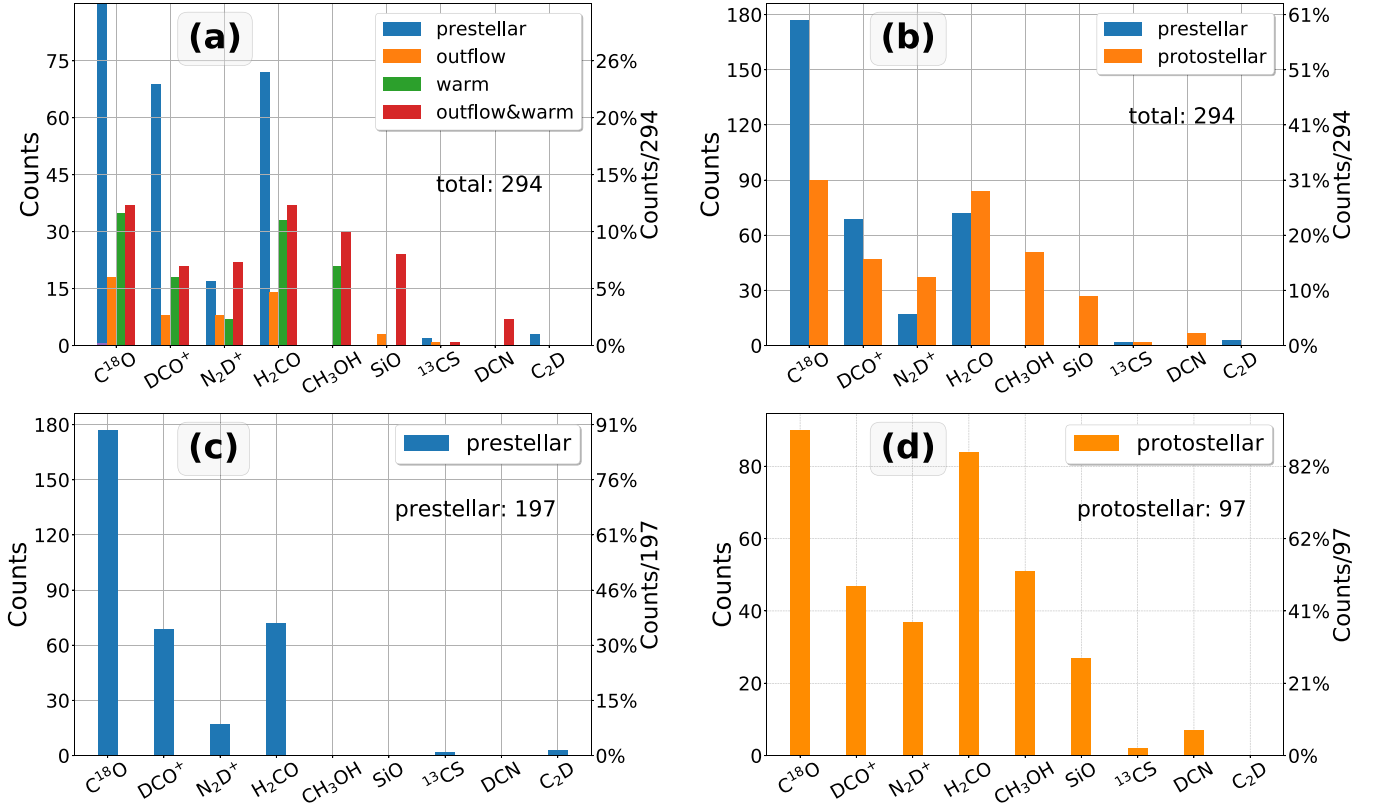
Figure 2. Histograms of the number and detection rate distributions of detected lines for: each evolutionary category of cores (a); prestellar vs. protostellar cores (b); prestellar cores only (c); and protostellar cores only (d).

Figure 2 shows histograms of the number distributions and detection rates of the detected lines for the prestellar cores, protostellar cores, and for each core category. N_2D^+ is detected in 17 prestellar cores and 37 protostellar cores, resulting in a detection rate in the prestellar phase ($9\% = 17/197$) lower than that in the protostellar phase ($38\% = 37/97$). The high N_2D^+ detection rate for the protostellar cores indicates that N_2D^+ does not exclusively trace prestellar cores and that it also frequently appears in protostellar cores (Giannetti et al. 2019). Among the detected deuterated molecules, DCO^+ has the highest detection rate in both the prestellar and protostellar cores. The DCO^+ detection rates are 35% ($69/197$) and 49% ($47/97$) for the prestellar and protostellar cores (Figure 2), respectively. This indicates that DCO^+ is more frequently detected than N_2D^+ in both the prestellar and protostellar cores.

The H_2CO detection rate in the protostellar cores ($87\% = 84/97$) is more than twice that in the prestellar cores ($37\% = 72/197$). On the other hand, H_2CO has a higher detection rate than N_2D^+ in both the prestellar and protostellar cores, indicating that H_2CO is more commonly seen than the N_2D^+ emission in these dense cores at early evolutionary phases. There are 51 ($53\% = 51/97$) protostellar cores showing CH_3OH line emission. DCN is detected in seven protostellar cores. C_2D is detected in three prestellar cores. ^{13}CS is detected in two prestellar and two protostellar cores. The detection numbers and detection rates of each line for all of the categories are summarized in Table 2.

3.2. Spatial Distributions of Line Emissions

In general, both CO and $C^{18}O$ show the most spatially extended emission over all clumps, followed by H_2CO and

CH_3OH, and then by DCO^+, N_2D^+, SiO, DCN, ^{13}CS, and C_2D. From Figure 1 (see also Appendix A), we note that the $C^{18}O$ emission is extended in the IRDC clumps. There is very weak $C^{18}O$ emission toward some of the dense cores, likely due to depletion (e.g., cores #28 and #30 in G14.49; see also Sabatini et al. 2022).

N_2D^+ shows extended emission toward dense cores. The peaks of the N_2D^+ emission are offset from the continuum peaks in some cores, with a significant decrease in intensity toward the continuum emission peaks (e.g., cores #8 and #2 in G14.49; see Figure 1). Both N_2 depletion and CO evaporation toward the centers of the cores can lead to a decrease in N_2D^+ abundance. We are unable to distinguish between these two possibilities with the current data. DCO^+ also shows extended emission toward the dense cores. However, the spatial distribution of DCO^+ does not always coincide with that of N_2D^+ (see, for example, Sakai et al. 2022). For instance, DCO^+ shows a significantly different spatial distribution from what is observed for N_2D^+ around cores #7, #10, and #21 in G14.49 (see Figure 1).

The peaks of the H_2CO and CH_3OH emission appear either to coincide with the continuum peaks or to be located in the direction of the outflows in the majority of cases (Figure 1 and Appendix A). The CH_3OH emission shows a behavior similar to what is observed for H_2CO, but with less extended emission. This is most likely due to the fact that the excitation conditions of H_2CO ($3_{0,3} - 2_{0,2}$) are different from those of CH_3OH (e.g., lower upper-level energies and critical densities; see Table 1).

There are some pairs of molecules that show similar spatial distributions in some clumps, e.g., H_2CO and CH_3OH. To compare the spatial trends of different species, we performed a

Table 2
Detection Rates

Molecules	Prestellar	Outflow Core	Protostellar Warm Core	Outflow + Warm Core	Sum	All
Total Number	197	21	37	37	97	294
$C^{18}O$	177 (89.8%)	18 (85.7%)	35 (94.6%)	37 (94.9%)	90 (92.8%)	267 (90.8%)
DCO^+	69 (35.0%)	8 (38.1%)	18 (48.6%)	21 (53.8%)	47 (48.5%)	116 (39.5%)
N_2D^+	17 (8.6%)	8 (38.1%)	7 (18.9%)	22 (56.4%)	37 (38.1%)	54 (18.4%)
H_2CO	72 (36.5%)	14 (66.7%)	33 (89.2%)	37 (94.9%)	84 (86.6%)	156 (53.1%)
CH_3OH	⋯	⋯	21 (56.8%)	30 (76.9%)	51 (52.6%)	51 (17.3%)
SiO	⋯	3 (14.3%)	⋯	24 (61.5%)	27 (27.8%)	27 (9.2%)
^{13}CS	2 (1.0%)	1 (4.8%)	⋯	1 (2.6%)	2 (2.1%)	4 (1.4%)
DCN	⋯	⋯	⋯	7 (17.9%)	7 (7.2%)	7 (2.4%)
C_2D	3 (1.5%)	⋯	⋯	⋯	⋯	3 (1.0%)

half-beam sampling for the 0th moment of each molecular line. Each data point (or pixel) is about half the beamwidth, to ensure that data points are not oversampled. The similarity of the 0th-moment maps of different molecules can be evaluated quantitatively by the cross correlation between each pair of maps, according to Guzmán et al. (2018):

$$\rho_{12} = \frac{\sum_{i,j} I_{1,ij}\, I_{2,ij}\, w_{ij}}{\left(\sum_{i,j} I_{1,ij}^2\, w_{ij} \sum_{i,j} I_{2,ij}^2\, w_{ij}\right)^{1/2}}, \quad (1)$$

where the sums are taken over all positions. $I_{1,ij}$ and $I_{2,ij}$ are the integrated intensities at the position i, j for two arbitrary species, 1 and 2, respectively, and the weight w_{ij} is equal to 0 or 1, depending on whether or not the line emission was detected at that position. ρ_{12} is equal to 1 if the 0th-moment maps of two molecules have the same spatial distribution. Although some pairs of molecules that show weak emission do not have statistically significant numbers of independent data points, they are still worth examining. To alleviate the effect of insufficient numbers of independent data points for comparison, we avoid deriving the correlation coefficients of pairs of molecules whose overlapping emitting areas are smaller than one synthesized beam.

Figure 3 presents cross-correlation coefficients for the 0th-moment maps for each pair of molecules. The correlation between N_2D^+ and DCO^+ is better than those for the other detected deuterated molecules (i.e., DCN and C_2D) in all the clumps. This is because the emitting regions of the DCN and C_2D lines are smaller than those for either N_2D^+ or DCO^+ (Figure 1). The DCO^+ line emission coincides better with H_2CO and CH_3OH than N_2D^+ in terms of spatial distribution. This may be because DCO^+, H_2CO, and CH_3OH have a common precursor molecule of CO that tends to destroy N_2D^+ (see Sections 4.2 and 4.3).

In general, the CH_3OH and H_2CO emissions have the most similar spatial distributions in integrated intensities, with the highest correlation coefficients among the detected lines. Most of the CH_3OH and H_2CO emissions appear to be around either outflows or dense cores (Figure 1). In addition, both the CH_3OH and H_2CO emissions show good spatial correlation with the SiO emission in most of the clumps (Figure 3). These results suggest that both the CH_3OH and H_2CO line emissions are closely related to the outflow activity toward protostellar cores in the ASHES clumps.

3.3. Molecular Line Parameters

Figure 4 shows the distribution of the derived I and σ_{obs} of each line for the prestellar and protostellar cores (see also Table 3). Overall, σ_{obs} shows no significant difference between the prestellar and protostellar cores for the $C^{18}O$ and DCO^+ emissions. This indicates that the protostellar cores are still at a very early evolutionary phase, in which the line widths of $C^{18}O$ (a low-density gas tracer) and DCO^+ (a high-density tracer) have not been significantly affected by protostellar activity. In general, the N_2D^+ line has a comparable I in both the prestellar and protostellar cores, except for four protostellar cores that present a relatively higher I than for the prestellar cores. On the other hand, the N_2D^+ line emission shows a relatively larger σ_{obs} in the protostellar cores compared with the prestellar cores. This might be because the N_2D^+ line emission toward the protostellar cores is influenced by the injection of turbulence, as a result of protostellar activity.

For the H_2CO emission, both I and σ_{obs} in the protostellar cores are higher than in the prestellar cores. This is because H_2CO abundances can be significantly enhanced in warm and dense environments, and its line width can be broadened by protostellar activity (e.g., outflows; Tafalla et al. 2010; Sakai et al. 2012). In addition, H_2CO is the molecule in our sample that shows a clearly increasing trend in both I and σ_{obs} for categories 1 to 4 (see Figure 4), indicating that its abundance and line width are sensitive to the evolution of the dense cores. This implies that H_2CO could be used as a diagnostic tool for inferring star formation activities.

From Figure 4, one notes that the H_2CO ($\langle\sigma_{obs}\rangle = 1.68$ km s^{-1}) and CH_3OH ($\langle\sigma_{obs}\rangle = 1.82$ km s^{-1}) lines show relatively larger σ_{obs} than $C^{18}O$ ($\langle\sigma_{obs}\rangle = 0.99$ km s^{-1}), DCO^+ ($\langle\sigma_{obs}\rangle = 0.35$ km s^{-1}), and N_2D^+ ($\langle\sigma_{obs}\rangle = 0.25$ km s^{-1}) toward the protostellar cores (see also Table 3). This could be because H_2CO and CH_3OH are associated with more turbulent gas components that are affected by protostellar activity (e.g., outflows; Tychoniec et al. 2021). We refrain from investigating I and σ_{obs} for the ^{13}CS, DCN, and C_2D emissions, due to the lack of a sufficient number of detections for a meaningful analysis, as well as the SiO emission, which is mainly associated with outflows.

3.4. Derivation of Physical Parameters

The rotational excitation temperature (T_{NH_3}) is derived from NH_3 (1, 1) and (2, 2) transition lines obtained from the CACHMC survey (Complete ATCA[16] Census of High-Mass Clumps; D. Allingham et al. 2022, in preparation) at ∼5″

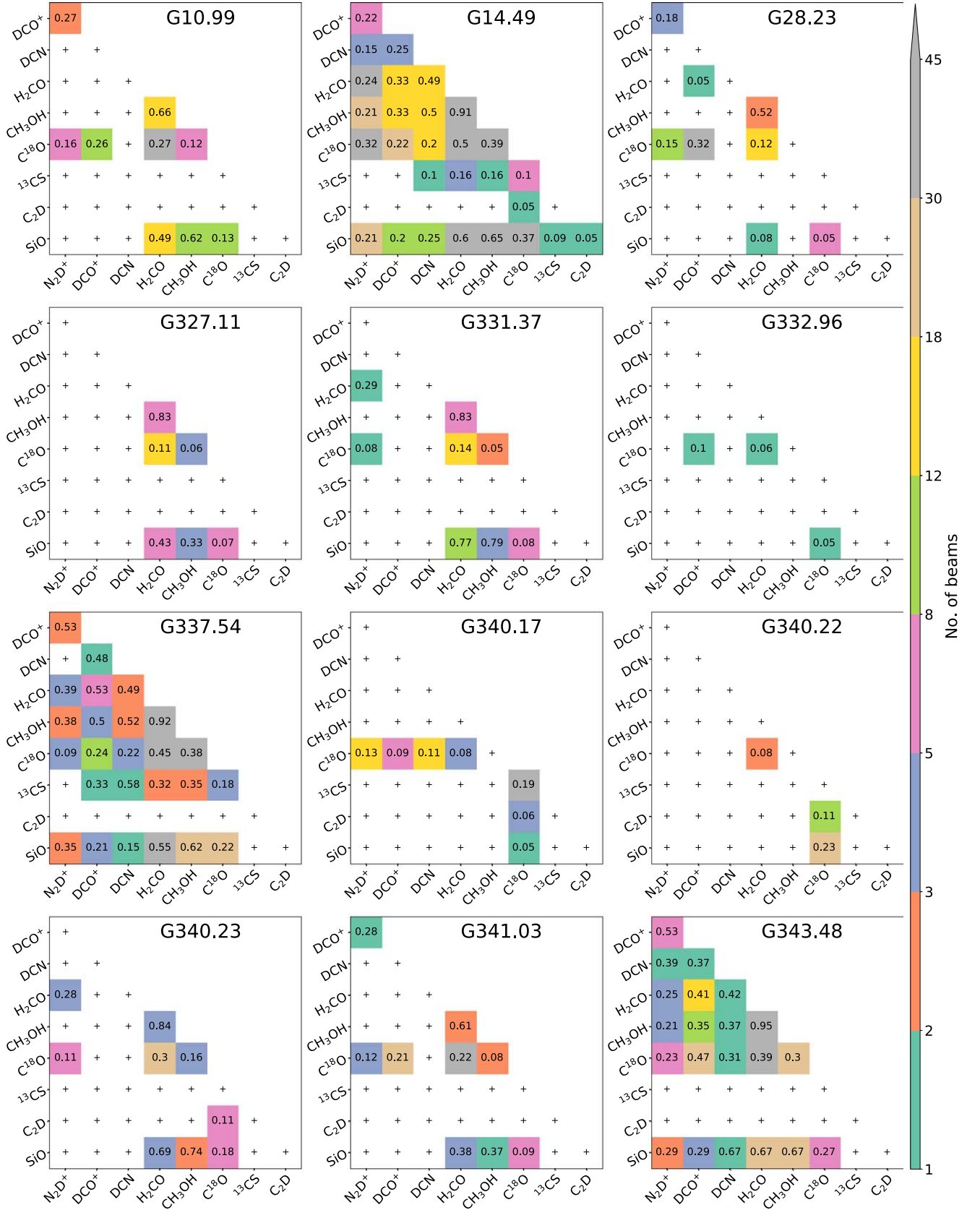[16] The Australia Telescope Compact Array.

Figure 3. Integrated intensity correlation matrix, showing cross correlations for each pair of molecules. The correlation coefficients are described in the text. The "+" symbols mean that correlation coefficients cannot be derived, either due to lack of detection or the spatially overlapped emitting area being smaller than one beam in size. The colors indicate the number of beam areas of the spatially overlapping emitting regions. Larger numbers of beam areas have more robust derived correlation coefficients than smaller ones.
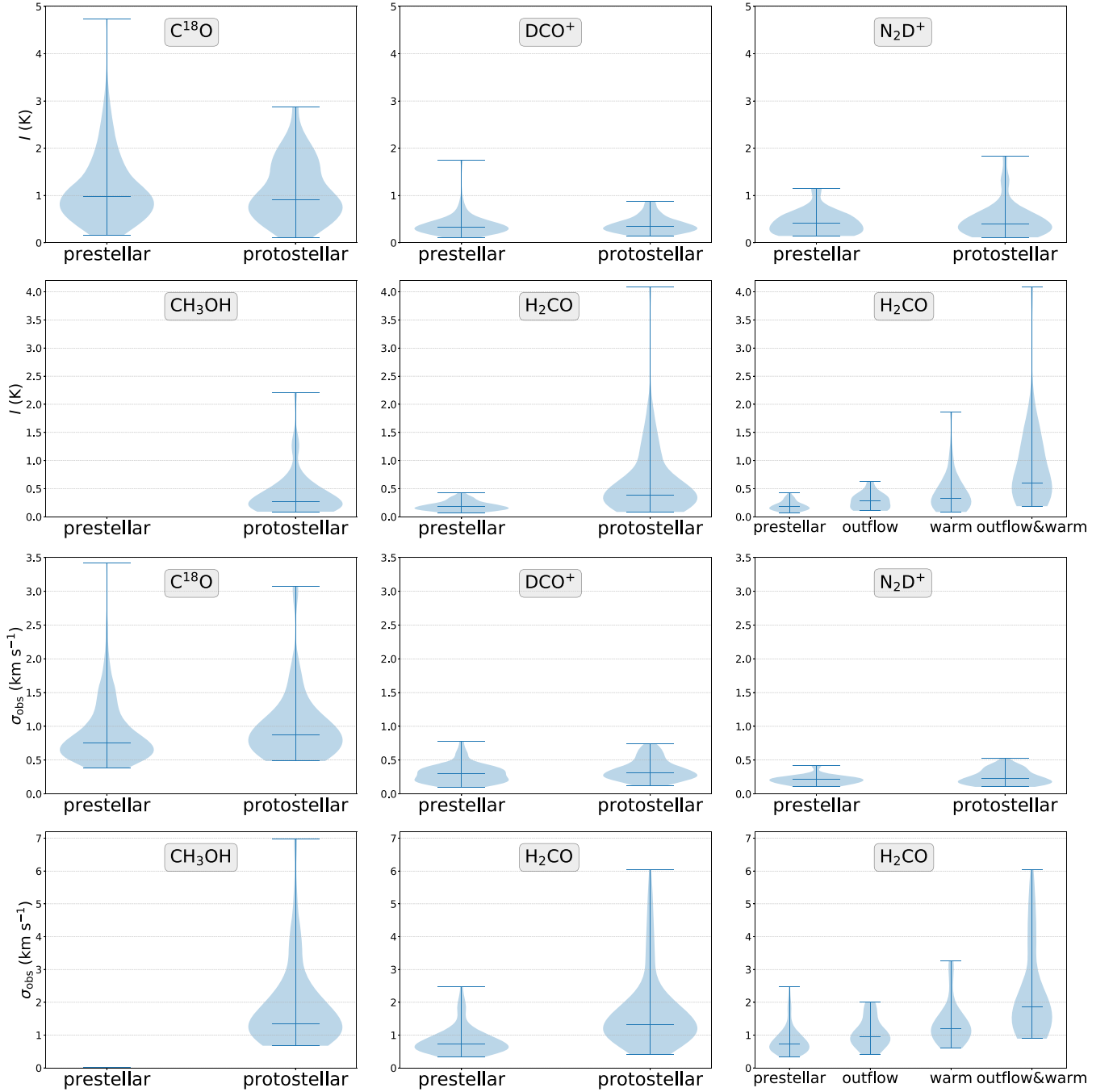
Figure 4. Violin plots of the peak intensity I and observed velocity dispersion $\sigma_{\rm obs}$ distributions for each line. The shape of each distribution shows the probability density of the data, smoothed by a kernel density estimator. The last panel shows the H_2CO peak intensity distributions of each category of dense cores. The blue horizontal bars from the top to bottom of each violin plot represent the maximum, mean, and minimum values, respectively.

angular resolution (see Appendix B for the detailed procedure for the excitation temperature determination). More details of the procedure for the temperature determination and the survey results will be presented in a forthcoming paper (D. Allingham et al. 2022, in preparation). The derived $T_{\rm NH_3}$ is used as the excitation temperature in the calculation of all molecular parameters, except for G332.96, which has no available NH_3 data. We used the dust temperature at the clump scale of 12.6 K for G332.96 (Paper I). The averaged temperatures of the dense cores in the same category for a given clump are used for those dense cores that have no available $T_{\rm NH_3}$. The approximation of using $T_{\rm NH_3}$ as the excitation temperature is based on the local

thermodynamic equilibrium (LTE) conditions in the calculation of the molecular density. The results could be highly sensitive to the choice of the excitation temperature.

Using these new temperatures, we have recalculated the ASHES cores properties. The analysis of how these new core properties affect the analysis presented in Paper I will be presented in a forthcoming paper (S. Li et al. 2022, in preparation). For the chemical analysis of the current work, we have used the updated core-averaged H_2 column densities and core volume densities (see Appendix C). The updated parameters are 4.9×10^{21}–2.0×10^{23} cm^{-2} for the core-averaged column density and 1.4×10^5–1.7×10^7 cm^{-3} for

Table 3
Median and Mean Values of the Derived Line Parameters for Each Category

Name	Prestellar		Protostellar										All	
			Outflow Core		Warm Core		Outflow + Warm Core		Sum					
	Median	Mean	Median	Mean	Median	Mean	Median	Mean	Median	Mean			Median	Mean
$I_{C^{18}O}$	0.98	1.12	0.81	0.88	0.86	0.96	1.22	1.30	0.90	1.09			0.93	1.11
$\sigma_{C^{18}O}$	0.75	0.89	0.88	0.95	0.92	1.02	0.85	0.97	0.88	0.99			0.79	0.92
$I_{N_2D^+}$	0.41	0.42	0.29	0.31	0.52	0.47	0.44	0.53	0.40	0.47			0.41	0.45
$\sigma_{N_2D^+}$	0.22	0.21	0.21	0.25	0.19	0.21	0.24	0.26	0.23	0.25			0.22	0.23
I_{DCO^+}	0.32	0.37	0.37	0.46	0.33	0.37	0.36	0.37	0.35	0.39			0.33	0.38
σ_{DCO^+}	0.29	0.30	0.29	0.29	0.38	0.39	0.32	0.35	0.32	0.35			0.30	0.32
σ_{CH_3OH}	⋯	⋯	⋯	⋯	1.23	1.59	1.46	1.98	1.35	1.82			1.35	1.82
I_{H_2CO}	0.18	0.19	0.28	0.28	0.33	0.42	0.61	0.88	0.38	0.60			0.26	0.41
σ_{H_2CO}	0.72	0.84	0.96	1.06	1.19	1.36	1.85	2.21	1.33	1.68			1.00	1.29
$I_{^{13}CS}$	0.38	0.38	0.27	0.27	⋯	⋯	0.18	0.18	0.22	0.22			0.28	0.30
$\sigma_{^{13}CS}$	0.34	0.34	0.46	0.46	⋯	⋯	1.30	1.30	0.88	0.88			0.42	0.61
I_{DCN}	⋯	⋯	⋯	⋯	⋯	⋯	0.26	0.22	0.26	0.22			0.26	0.22
σ_{DCN}	⋯	⋯	⋯	⋯	⋯	⋯	1.21	1.04	1.21	1.04			1.21	1.04
I_{C_2D}	0.22	0.24	⋯	⋯	⋯	⋯	⋯	⋯	⋯	⋯			0.22	0.24
σ_{C_2D}	0.13	0.17	⋯	⋯	⋯	⋯	⋯	⋯	⋯	⋯			0.13	0.17

Note. The units are K and km s^{-1} for peak intensity and observed line width, respectively.

the core-averaged volume density. The protostellar cores have higher column densities and volume densities than the prestellar cores (Table 4).

Assuming LTE and optically thin molecular emission, the molecular column density (N_{mol}) can be estimated from the velocity-integrated intensity (see Appendix C for a detailed derivation of the column density). To study the properties of the molecules, we also calculated the molecular abundances, $X_{mol} = N_{mol}/N_{H_2}$, using the updated H_2 column density and the derived molecular column densities.

The derived N_2D^+ column densities range from 5.9×10^{10} to 1.3×10^{12} cm^{-2}, resulting in N_2D^+ abundances of 2.2×10^{-12}–1.7×10^{-11}. The N_2D^+ column densities are similar to the value of 6.2×10^{11} cm^{-2} obtained for other IRDCs (e.g., Chen et al. 2010; Gerner et al. 2015; Barnes et al. 2016), and the N_2D^+ abundances are comparable to the values of $\sim 10^{-12}$ in other massive clumps (Giannetti et al. 2019). The estimated DCO^+ column densities are between 4.7×10^{10} and 6.5×10^{11} cm^{-2}, leading to DCO^+ abundances of 1.3×10^{-12}–2.4×10^{-11}. N_{DCO^+} is similar to the values reported in other IRDCs ($\leqslant 3 \times 10^{11}$ cm^{-2}; Gerner et al. 2015). The derived DCN column densities and abundances are 2.7×10^{11}–2.0×10^{12} cm^{-2} and 5.6×10^{-12}–1.2×10^{-11}, respectively. The DCN abundances are significantly lower than those in more evolved dense cores in W3 ($>10^{-10}$; Mottram et al. 2020). C_2D has column densities of 4.8×10^{12}–1.1×10^{13} cm^{-2} and abundances of 1.5×10^{-10}–4.2×10^{-10}.

Given that these dense cores are still in very early evolutionary phases and are characterized by a cold environment, H_2CO is expected to form in ice on the grain surface and to subsequently be released to the gas phase (Jørgensen et al. 2005). We assumed an ortho-to-para ratio of 1.6, which is consistent with thermalization at a low temperature of $T \sim 15$ K (Jørgensen et al. 2005). The derived H_2CO column densities and abundances are 4.1×10^{11}–9.3×10^{13} cm^{-2} and 1.2×10^{-11}–1.1×10^{-9}, respectively.

CH_3OH has column densities of 2.4×10^{12}–1.9×10^{14} cm^{-2} and abundances of 7.3×10^{-11}–2.3×10^{-9} for the detected dense cores. The abundances of H_2CO and CH_3OH are similar to those in dense cores prior to the hot-core phase in other IRDCs (a few 10^{-10} for H_2CO and CH_3OH; Gerner et al. 2014; Mottram et al. 2020), but lower than those in hot-core and UCHII regions ($\geqslant 10^{-9}$; e.g., Gerner et al. 2014; Mottram et al. 2020).

A $C^{18}O$ optical correction factor, $C_\tau = \tau_{C^{18}O}/[1 - \exp(-\tau_{C^{18}O})]$, is applied in the calculation of the $C^{18}O$ column density. C_τ is derived following the approach described in Sabatini et al. (2019). The detailed estimation of the $C^{18}O$ correction factor is presented in Sabatini et al. (2022). The calculated $C^{18}O$ column densities vary from 1.3×10^{14} to 5.6×10^{15} cm^{-2}, resulting in $C^{18}O$ abundances of 3.7×10^{-9}–4.8×10^{-7}. The estimated SiO column densities vary from 2.3×10^{11}–3.2×10^{13} cm^{-2}, which are comparable to the values in the outflows, whereas the derived abundances of 3.0×10^{-12}–3.4×10^{-10} are lower than those found in the outflows ($\geqslant 1.1 \times 10^{-9}$; see Paper II).

Figure 5 shows histograms of the molecular column densities and abundance ratio distributions for the prestellar and protostellar cores (see also Table 4). Except for $C^{18}O$ and N_2D^+, which have similar column densities in the prestellar and protostellar cores, all other molecules have column densities in the prestellar cores that are relatively lower than those in the protostellar cores. On the other hand, the N_2D^+, DCO^+, and $C^{18}O$ abundances are higher in the prestellar cores than in the protostellar cores, indicating that the abundances of these molecules tend to decrease with the evolution of the dense cores. These abundance variations are dominated by the effect of the rapid H_2 density increase from the prestellar to protostellar phases (see Section 4.2). In contrast, the abundance of H_2CO in the protostellar cores is higher than in the prestellar ones, suggesting that its abundance can be enhanced with core evolution.

Table 4
Median and Mean values of the Derived Core Properties for Each Category

| Name	Prestellar		Outflow Core		Warm Core		Outflow + Warm Core		Sum		All	
						Protostellar						
	Median	Mean	Median	Mean	Median	Mean	Median	Mean	Median	Mean	Median	Mean
T_{NH_3}(K)	14.1	14.2	12.8	13.8	14.8	14.3	15.3	14.9	14.8	14.4	14.4	14.3
Core-averaged volume densities (cm^{-3}) and averaged column densities (cm^{-2})												
n_{H_2}	1.06E+06	1.51E+06	1.52E+06	2.50E+06	1.20E+06	2.69E+06	3.42E+06	5.28E+06	2.30E+06	3.69E+06	1.25E+06	2.23E+06
N_{H_2}	2.10E+22	2.56E+22	3.25E+22	3.83E+22	2.57E+22	4.15E+22	5.64E+22	7.91E+22	4.36E+22	5.59E+22	2.56E+22	3.56E+22
Column Densities (cm^{-2})												
$N_{C^{18}O}$	1.10E+15	1.42E+15	8.35E+14	1.30E+15	1.18E+15	1.54E+15	1.79E+15	2.20E+15	1.29E+15	1.77E+15	1.16E+15	1.54E+15
$N_{N_2D^+}$	2.63E+11	3.30E+11	2.28E+11	2.61E+11	3.55E+11	4.06E+11	2.96E+11	4.39E+11	2.74E+11	3.94E+11	2.72E+11	3.74E+11
N_{DCO^+}	1.47E+11	1.89E+11	1.71E+11	2.12E+11	2.22E+11	2.37E+11	1.92E+11	2.05E+11	1.92E+11	2.18E+11	1.67E+11	2.01E+11
N_{CH_3OH}	...	...	...	...	8.36E+12	2.09E+13	1.86E+13	3.61E+13	1.74E+13	2.98E+13	1.74E+13	2.98E+13
N_{H_2CO}	1.39E+12	1.61E+12	2.84E+12	3.00E+12	4.29E+12	5.83E+12	1.20E+13	2.04E+13	6.11E+12	1.18E+13	2.43E+12	7.09E+12
$N_{^{13}CS}$	1.14E+12	1.14E+12	1.06E+12	1.06E+12	...	...	1.89E+12	1.89E+12	1.47E+12	1.47E+12	1.29E+12	1.31E+12
N_{DCN}	...	...	...	...	...	...	7.73E+11	1.05E+12	7.73E+11	1.05E+12	7.73E+11	1.05E+12
N_{C_2D}	8.91E+12	8.33E+12	...	...	...	...	...	...	...	...	8.91E+12	8.33E+12
N_{SiO}	...	...	1.74E+12	1.46E+12	...	...	1.70E+12	5.59E+12	1.74E+12	5.13E+12	1.74E+12	5.13E+12
Molecular Abundances												
$X_{C^{18}O}$	4.95E-08	6.74E-08	3.53E-08	3.68E-08	3.85E-08	6.37E-08	2.33E-08	2.95E-08	2.99E-08	4.43E-08	4.23E-08	5.96E-08
$X_{N_2D^+}$	7.57E-12	8.07E-12	5.94E-12	5.99E-12	7.78E-12	7.91E-12	4.90E-12	5.07E-12	5.23E-12	5.81E-12	6.12E-12	6.52E-12
X_{DCO^+}	5.23E-12	5.95E-12	4.79E-12	4.71E-12	6.58E-12	7.60E-12	2.46E-12	2.84E-12	4.02E-12	4.98E-12	4.78E-12	5.56E-12
X_{CH_3OH}	...	...	...	...	2.75E-10	4.44E-10	3.00E-10	4.72E-10	2.83E-10	4.60E-10	2.83E-10	4.60E-10
X_{H_2CO}	5.20E-11	6.88E-11	8.09E-11	8.74E-11	1.59E-10	2.40E-10	1.76E-10	2.80E-10	1.53E-10	2.32E-10	8.87E-11	1.57E-10
$X_{^{13}CS}$	6.03E-11	6.03E-11	7.94E-11	7.94E-11	...	...	1.52E-11	1.52E-11	4.73E-11	4.73E-11	5.41E-11	5.38E-11
X_{DCN}	...	...	...	...	...	...	8.30E-12	8.55E-12	8.30E-12	8.55E-12	8.30E-12	8.55E-12
X_{C_2D}	1.79E-10	2.50E-10	...	...	...	...	...	...	...	...	1.79E-10	2.50E-10
X_{SiO}	...	...	4.05E-11	4.38E-11	...	...	3.26E-11	5.69E-11	3.35E-11	5.54E-11	3.35E-11	5.54E-11
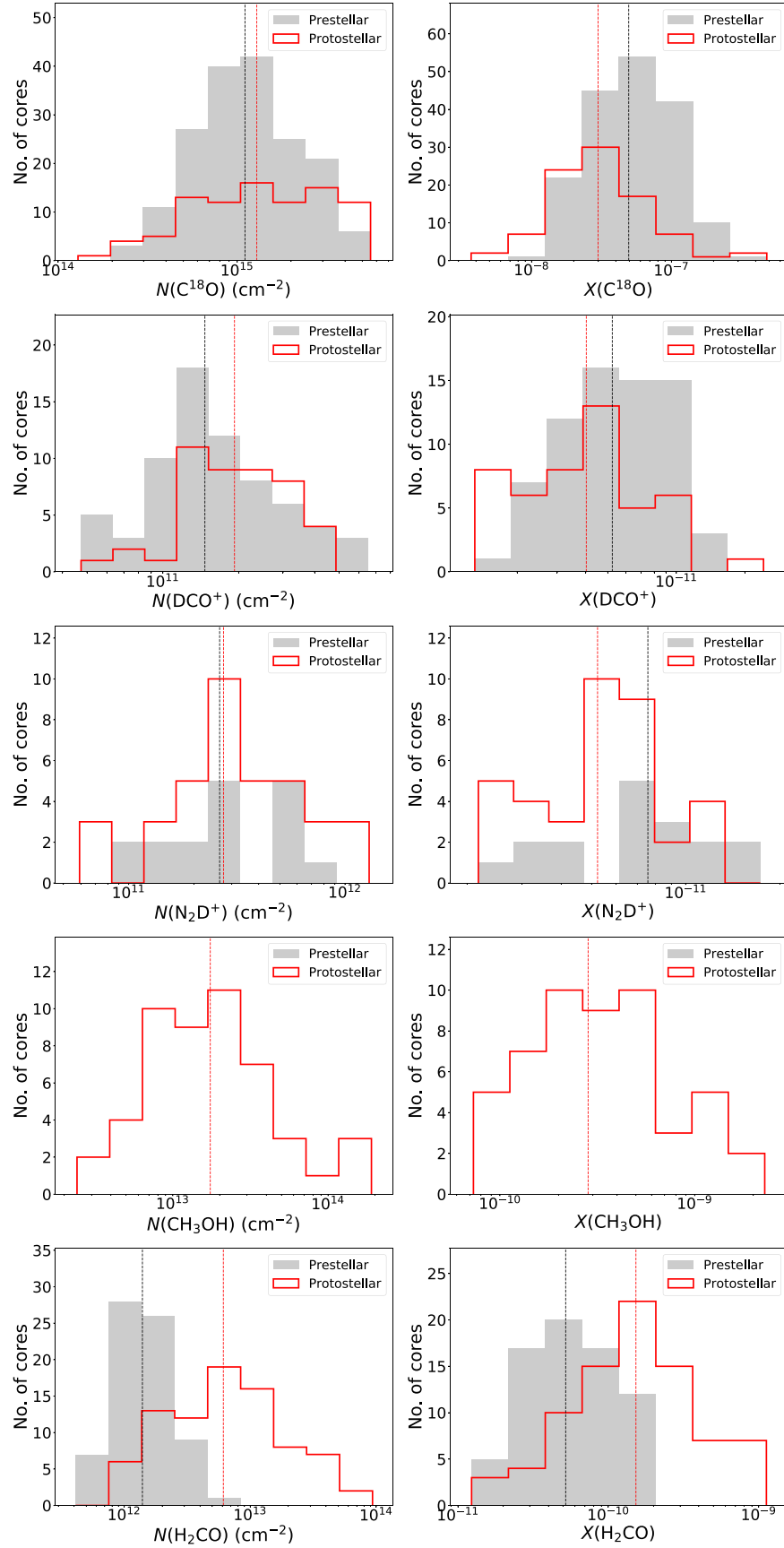
Figure 5. Left column: histograms of the molecular column densities for the prestellar and protostellar cores. Right column: histograms of the molecular abundances for the prestellar and protostellar cores. The black dashed vertical lines indicate the median values of the parameters.

4. Discussion

4.1. Missing Flux

To understand the impact of the missing flux on the line emission, we compared the 12m7m and 12m7mTP data sets. We investigated the integrated intensities, peak intensities, line widths, and central velocities of the line emissions between the two data sets.

For the N_2D^+ line emission, we find that the 12m7m data have recovered about 92% of the 12m7mTP flux. The differences of the measured I and σ_{obs} are factors of 0.94 and 0.99, respectively. For the DCO^+ line emission, the mean ratios of 12m7m to 12m7mTP are 0.89 for I and 0.9 for σ_{obs}, resulting a mean flux ratio (velocity-integrated intensity) of 0.79. The DCO^+ emission behavior is very similar to that of N_2D^+. These results indicate that most of the N_2D^+ and DCO^+ emission is compact and recovered without the addition of TP data from single-dish telescopes.

For the H_2CO $(3_{0,3} - 2_{0,2})$ line emission, the 12m7m data recover about 71% of the 12m7mTP flux, and the mean ratios of 12m7m to 12m7mTP for I and σ_{obs} are 0.82 and 0.87, respectively. On the other hand, CH_3OH has similar flux, I, and σ_{obs} between the 12m7m and 12m7mTP data sets; the mean ratio (12m7m/12m7mTP) is 0.94 for flux, 0.94 for I, and 1.0 for σ_{obs}. This indicates that CH_3OH traces more spatially compact emission compared with H_2CO. This suggests that the observed CH_3OH transition may preferentially be concentrated near the protostars or in knots in outflows.

For $C^{18}O$, the mean ratios of the 12m7m to 12m7mTP data are 0.54 for the intensity peak and 0.7 for the velocity dispersion, resulting in a mean flux ratio of 0.36. Among the detected lines (excluding CO), $C^{18}O$ suffers most severely from missing flux. This indicates that $C^{18}O$ probes a significant amount of diffuse molecular gas. For the remaining lines with relatively low detection rates, their 12m7m images are weakly affected by the missing flux. The mean flux ratios of 12m7m to 12m7mTP are 1.0 for SiO, 0.96 for ^{13}CS, 0.9 for DCN, and 0.98 for C_2D.

4.2. Deuterated Molecules

N_2D^+ is expected to be abundant in cold (<20 K) and dense ($\sim10^5$ cm^{-3}) regions, in which its major destroyer, CO, is significantly depleted onto grain surfaces. N_2D^+ can be formed via N_2 reacting with H_2D^+ (dominant reaction: $N_2 + H_2D^+ \rightarrow N_2D^+ + H_2$), D_2H^+, or D_3^+ (Pagani et al. 2009), and destroyed by CO ($N_2D^+ + CO \rightarrow DCO^+ + N_2$) or electrons ($N_2D^+ + e^- \rightarrow ND + N$ or $D + N_2$; Sakai et al. 2022). DCO^+ is also considered to be a cold and dense gas tracer. However, DCO^+ requires gas-phase CO for its formation at cold temperatures ($T < 20$–50 K), i.e., $H_2D^+ + CO \rightarrow DCO^+ + H_2$ (Wootten & Loren 1987). Therefore, the DCO^+ abundance does not decrease rapidly when CO is released to the gas phase from the grain mantles (Dalgarno & Lepp 1984). The different chemistry between N_2D^+ and DCO^+ may explain their different spatial distributions as seen in Figure 1 (e.g., Sakai et al. 2022). DCN and C_2D tend to form in warm environments (Turner 2001; Albertsson et al. 2013).

The N_2D^+ and DCO^+ column densities exhibit a strong correlation (see Figure 15 in Appendix A), with a Spearman rank correlation coefficient[17] of $r = 0.58$. This is mostly
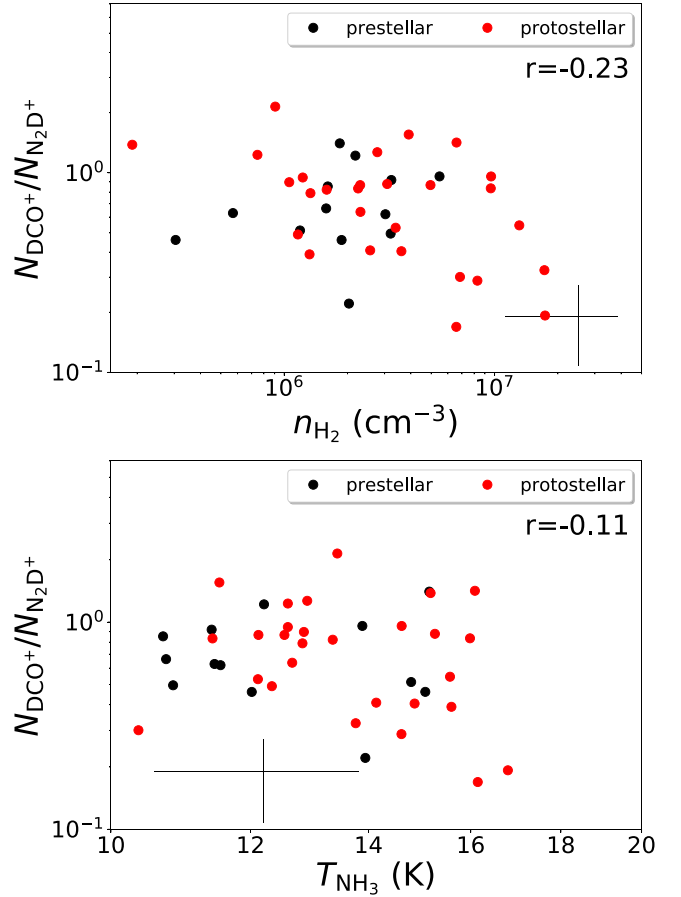
---

[17] Spearman's rank correlation test is a nonparametric measure of the monotonicity of the relationship between two variables. A correlation coefficient $|r| \geqslant 0.5$ means strong correlation, $0.5 > |r| \geqslant 0.3$ means moderate correlation, $0.3 > |r| \geqslant 0.1$ means weak correlation, and $0.1 > |r|$ means no correlation (Cohen 1988).
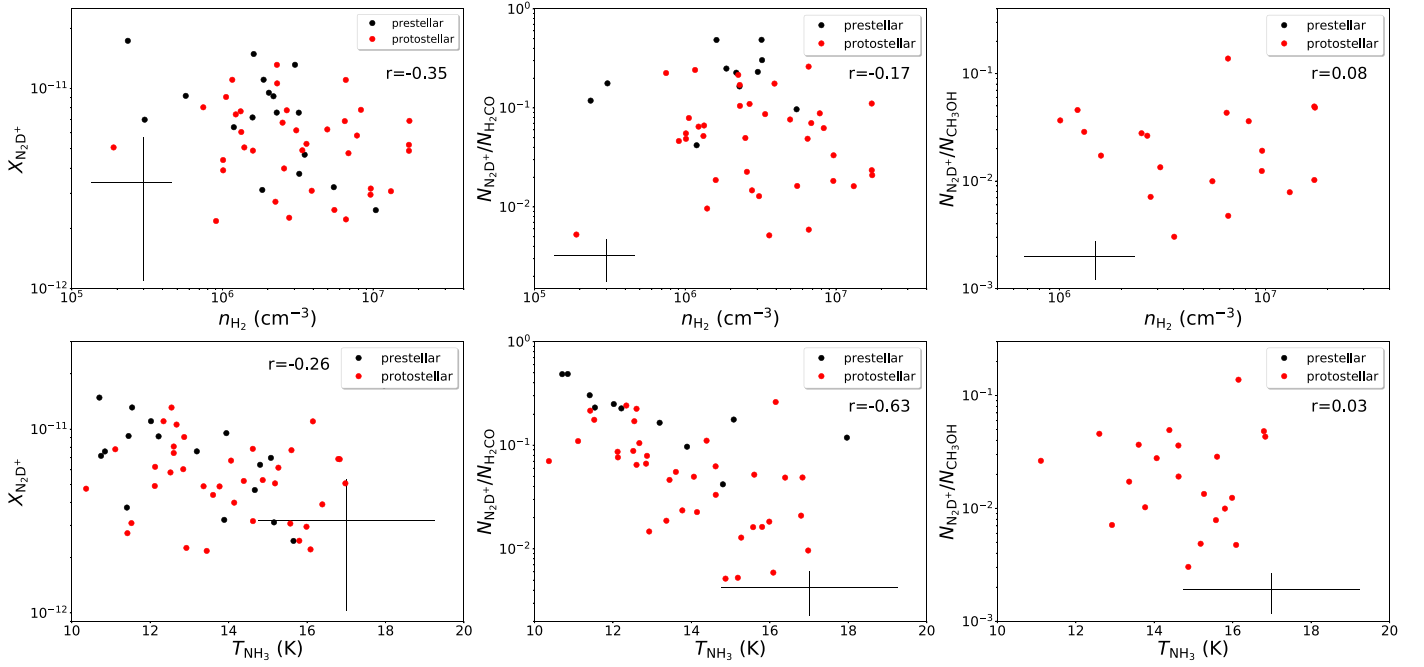

Figure 6. The column density ratio of DCO^+ to N_2D^+ vs. the core-averaged volume density n_{H_2} and temperature T_{NH_3}.

because both lines trace cold and dense gas in the dense cores. The N_2D^+ abundance appears to decrease with increasing volume densities n_{H_2}, with a moderate correlation coefficient of -0.35 (see Figure 7). As mentioned in Section 3.4, the volume density increases with the evolution of the dense cores, which continue to accumulate mass via the accretion of material from natal clumps. The n_{H_2}–$X_{N_2D^+}$ anticorrelation suggests that the N_2D^+ abundance decreases with core evolution. As the cores evolve, the gas temperature increases, thereby lowering the deuterium enhancement. In this case, one naively expects an anticorrelation between the N_2D^+ abundance and T_{NH_3}. As seen in Figure 7, there is no obvious trend between the N_2D^+ abundance and T_{NH_3}. These cores are still very cold, with temperatures between 10 and 20 K, which are lower than the sublimation temperature of CO (~25 K). This may explain why the N_2D^+ abundance does not vary significantly with T_{NH_3}. In addition, this suggests that these cores are still at a very early evolutionary phase, in which the surrounding environment has not been significantly warmed up by young stellar objects. On the other hand, we cannot completely rule out the possibility that T_{NH_3} does not accurately reflect the true temperature of the dense molecular gas traced by N_2D^+, because the spatial resolution of T_{NH_3} ($\sim5''$) is coarser than the ALMA observations ($\sim1.''2$) and the critical density of NH_3 (1,1) is only of a few 10^4 cm^{-3}. Determinations of temperatures at $\sim1''$ scales would be necessary to verify whether the T_{NH_3} varies significantly down to the small scale. The n_{H_2}–$X_{N_2D^+}$ and $X_{N_2D^+}$–T_{NH_3} results

Figure 7. Top row: plots of N_{H_2} vs. $N_{N_2D^+}$, $N_{N_2D^+}/N_{H_2CO}$, and $N_{N_2D^+}/N_{CH_3OH}$. Bottom row: plots of T_{NH_3} vs. $X_{N_2D^+}$, $N_{N_2D^+}/N_{H_2CO}$, and $N_{N_2D^+}/N_{CH_3OH}$. The correlation coefficients derived from Spearman's rank correlation test are given in the text in each panel. The black cross shows the typical uncertainty in each panel.
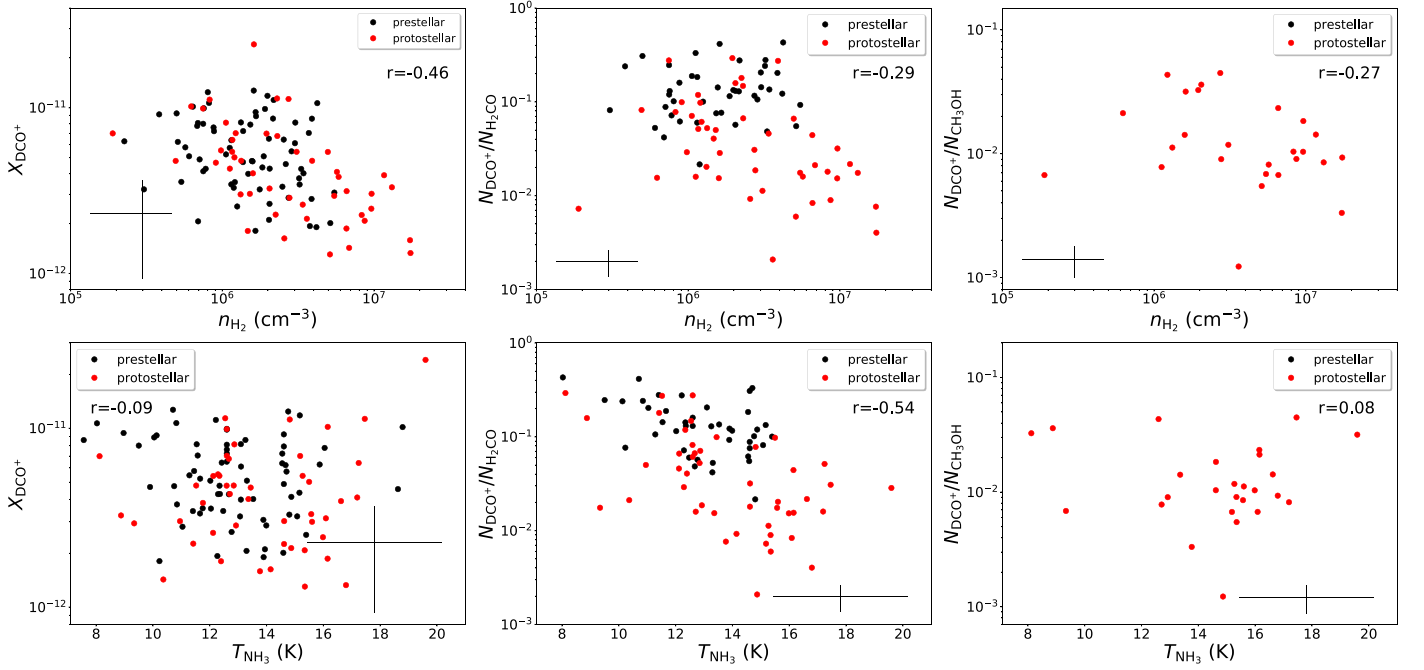

Figure 8. The same as Figure 7, but for DCO$^+$.

suggest that the N_2D^+ abundance variation is dominated by the H_2 core density in the ASHES sample.

The column density ratio of $N_{N_2D^+}/N_{H_2CO}$ appears to decrease as a function of increasing n_{H_2}. However, a closer look reveals that this weak anticorrelation is mostly dominated by the protostellar cores. Both $N_{N_2D^+}$ and N_{H_2CO} tend to increase with n_{H_2}, and therefore the $N_{N_2D^+}/N_{H_2CO}$-n_{H_2} anticorrelation implies that N_{H_2CO} is more sensitive to n_{H_2} than $N_{N_2D^+}$ toward the protostellar cores (see also Section 3.3). In addition, the $N_{N_2D^+}/N_{H_2CO}$ ratio also appears to decrease with increasing

T_{NH_3}, with a correlation coefficient of -0.63. This is because the H_2CO abundance is enhanced by elevated temperatures. The $N_{N_2D^+}/N_{CH_3OH}$ ratio shows no clear trend with n_{H_2} or T_{NH_3}. In general, DCO$^+$ shows a similar trend to those seen in N_2D^+, except for n_{H_2}–N_{DCO^+}/N_{CH_3OH} ($r = -0.27$), which presents a weak anticorrelation. The difference in N_2D^+ and DCO$^+$ may be a result of different chemistry.

There is a weak anticorrelation between n_{H_2} and the $N_{DCO^+}/N_{N_2D^+}$ ratio (see Figure 6), with a correlation coefficient of $r = -0.23$. From Figures 7 and 8, one notes

that both the N_2D^+ and DCO^+ abundances decrease with increasing n_{H_2}, thereby causing the ratio of DCO^+ to N_2D^+ to change slightly with n_{H_2}. In addition, the $N_{DCO^+}/N_{N_2D^+}$ ratio shows only minor changes with T_{NH_3}, which gives a correlation coefficient of $r = -0.11$. This can be ascribed to the fact that the both DCO^+ and N_2D^+ abundances do not vary significantly with T_{NH_3} (see Figures 7 and 8).

4.3. H₂CO and CH₃OH

CH_3OH is considered to be mostly formed on the surface of dust grains, via the hydrogenation of CO with some intermediate products (e.g., H_2CO; Charnley et al. 1997; Watanabe et al. 2004; Fuchs et al. 2009):

$$CO \xrightarrow{H} HCO \xrightarrow{H} H_2CO \xrightarrow{H} CH_2OH,$$
$$CH_3O \xrightarrow{H} CH_3OH. \quad (2)$$
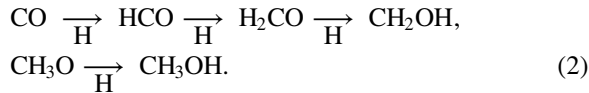
Unlike CH_3OH, which forms entirely on the surfaces of dust grains, H_2CO can be formed efficiently through both grain surface reaction in cold environments and gas-phase reactions in warm/hot environments (Le Teuff et al. 2000; Garrod et al. 2006; Fuchs et al. 2009).

CH_3OH shows a dip in its emission distribution at the center of some dense cores, such as the protostellar core #15 in G337.54 (Appendix A). A similar feature has been observed in low-mass prestellar cores, e.g., L1498 and L1517B (Tafalla et al. 2006). These authors suggest that the weaker CH_3OH emission toward the center of the dense cores is due to the significant CH_3OH depletion in cold and dense environments. Therefore, the low detection rate of CH_3OH in dense cores may be partly ascribed to CH_3OH depletion.

Among the detected molecules, the H_2CO and CH_3OH column densities show the strongest correlation, with correlation coefficients of 0.83 (see Figure 15 in Appendix A). As mentioned in Section 3.3, both H_2CO and CH_3OH tend to probe dense and high-velocity molecular gas, and hence the protostellar activity may be partly responsible for the strong correlation of the two species. For example, outflows/shocks can release both H_2CO and CH_3OH from grain mantles to the gas phase. In addition, both the H_2CO and CH_3OH column densities show strong correlations with the SiO column density (see Figure 15 in Appendix A); the correlation coefficient is 0.73 for $N_{H_2CO}-N_{SiO}$ and 0.84 for $N_{CH_3OH}-N_{SiO}$.

The derived abundance ratios of $H_2CO/CH_3OH = 0.1-2.3$ are comparable to the values of 0.9–2.5 reported in dense clumps ($n_{H_2} \sim 10^6$ cm^{-3}; Leurini et al. 2010), hot corinos (0.7–4.3; Maret et al. 2004, 2005), and low-mass starless cores (1.1–2.2, e.g., L1498 and L1517B; Tafalla et al. 2006). These values are higher than the abundance ratios derived in hot cores (0.13–0.28; Bisschop et al. 2007) and the shocked gas in the Galactic Center clouds (0.01–0.1; Requena-Torres et al. 2006; Lu et al. 2021), whereas they are significantly lower than those in the interclump medium ($H_2CO/CH_3OH = 14-1400$; $n_{H_2} \sim 10^4$ cm^{-3}; Leurini et al. 2010). The discrepancies could be attributed to either different dominant formation mechanisms or different chemical conditions. A detailed chemical modeling and observational comparison is needed to distinguish between these possibilities, which is beyond the scope of this paper.

5. Conclusion

In this paper, we analyze ALMA data from the ASHES project to investigate the chemistry of 294 dense cores in 12 massive 70 μm dark clumps. We have studied the spatial distributions and chemical variations of $C^{18}O$, DCO^+, N_2D^+, DCN, C_2D H_2CO, CH_3OH, ^{13}CS, and SiO in different evolutionary phases of dense cores. The main results are summarized below.

1. The detection rates of the DCO^+ emission in the prestellar and protostellar cores are higher than those for N_2D^+, whereas N_2D^+ is more sensitive to core evolution than DCO^+ in terms of clear variations of σ_{obs}. The commonly detected DCO^+ emission toward deeply embedded dense cores suggests that it is a good tracer of prestellar (detection rate: 35%) and early-phase protostellar cores (detection rate: 49%). On the other hand, we find that N_2D^+ does not exclusively trace the prestellar cores and that it is more frequently detected in the relatively earlier phase of the protostellar cores; the detection rate is 9% for the prestellar cores and 38% for the protostellar cores. This suggests that N_2D^+ is not the best tracer of prestellar cores at the sensitivity obtained in ASHES.

2. Both the N_2D^+ and DCO^+ abundances decrease with core evolution. This is mainly caused by the effects of the H_2 density increasing rapidly and the temperature increasing slowly from the prestellar to the protostellar phases in the identified cores. This can also explain why the $C^{18}O$ abundance is higher in the prestellar cores than in the protostellar cores.

3. The detection rate of the H_2CO emission toward dense cores is 52%, three times higher than that of CH_3OH (17%). The high detection rates of H_2CO in both the prestellar (37%) and protostellar cores (87%) suggest that H_2CO is commonly seen in the very early evolutionary phase. The line widths of H_2CO are higher than those for $C^{18}O$, N_2D^+, and DCO^+ toward the protostellar cores, which is likely due to the fact that the H_2CO line is associated with more turbulent gas components relating to protostellar activities (e.g., outflows). The H_2CO abundances are found to increase with the evolutions of the dense cores, as well as the line intensity and line width of the H_2CO $(3_{0,3}-2_{0,2})$ transition. These results indicate that H_2CO could be used as a diagnostic tool for inferring star formation activities.

Facility: ALMA.

Software: CASA (McMullin et al. 2007), APLpy (Robitaille & Bressert 2012), Astropy (Astropy Collaboration et al. 2013), Matplotlib (Hunter 2007), PySpecKit (Ginsburg et al. 2022).

Appendix A
Additional Figures and Table

Figure 9 shows the core-averaged spectra of the detected molecular lines in G14.49 as examples. Figures 10–14 show velocity-integrated intensity maps of the N_2D^+, DCO^+, DCN, H_2CO, CH_3OH, and $C^{18}O$ line emissions for each clump. Figure 15 shows the correlation of each pair of molecular column
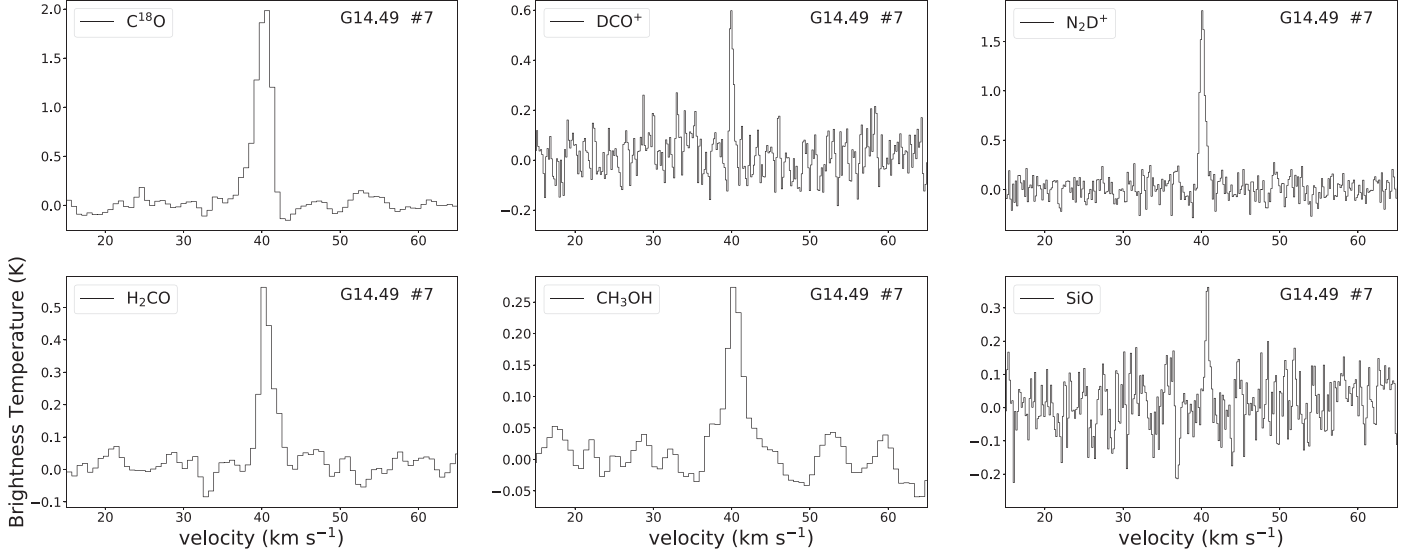
Figure 9. Examples of core-averaged spectra of $C^{18}O$, DCO^+, N_2D^+, H_2CO, CH_3OH, and SiO for core #7 in G14.49.
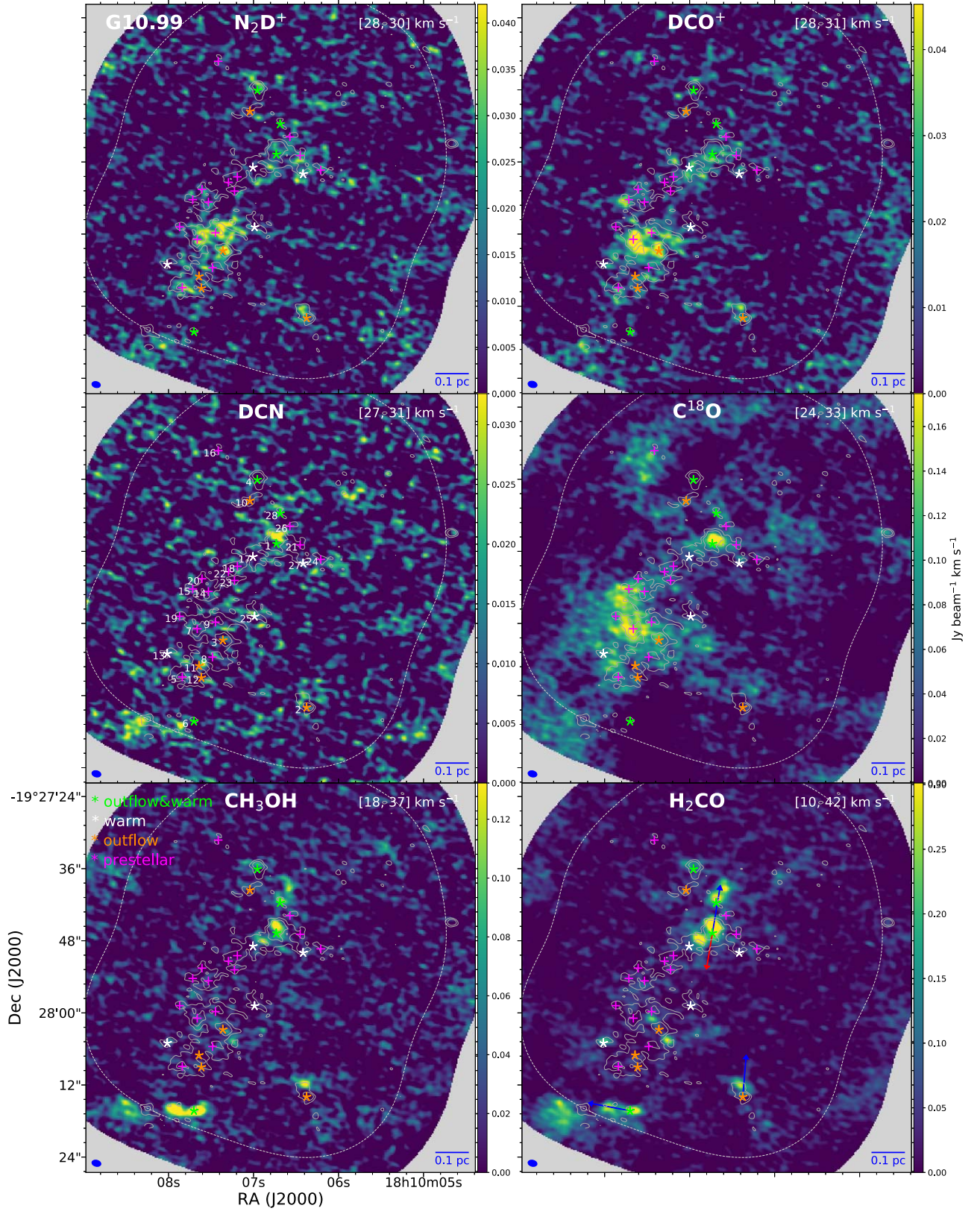
Figure 10. Velocity-integrated intensity maps of the N_2D^+, DCO^+, DCN, $C^{18}O$, CH_3OH, and H_2CO emission lines toward G10.99. The fuchsia pluses and the yellow, white, and green asterisk symbols indicate prestellar candidates (category 1), outflow cores (category 2), warm cores (category 3), and outflow + warm cores (category 4). The dashed white line shows 30% of the sensitivity level of the mosaic in the ALMA continuum image. The blue and red arrows in middle right panel indicate the directions of the blueshifted and redshifted CO outflow lobes (see Paper II), respectively. The gray contours in each panel shows the 1.3 mm continuum emission. The contour levels are $(3, 6) \times \sigma$, with $\sigma = 0.115$ mJy beam^{-1}. The beam size is shown in the lower left corner of each panel.
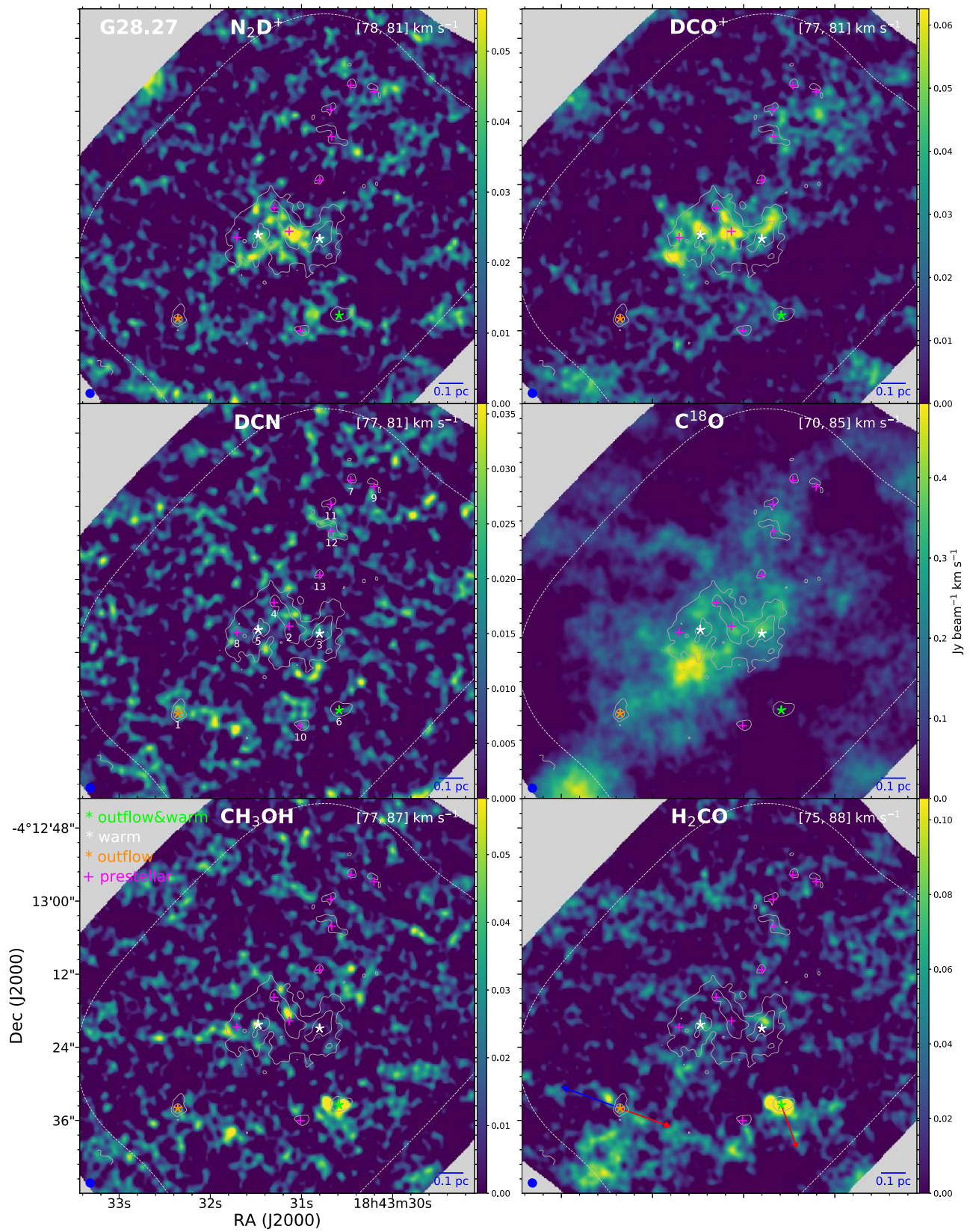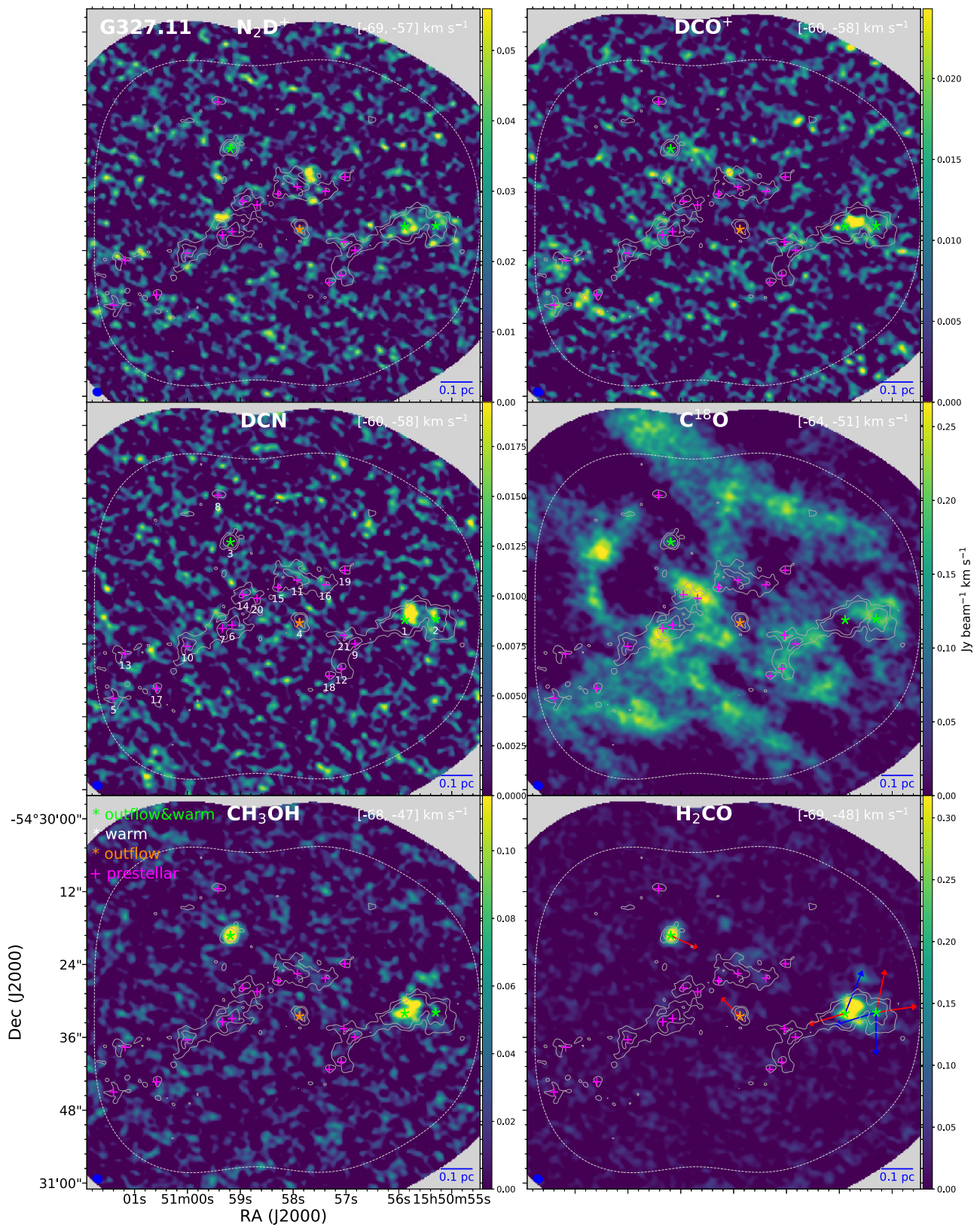
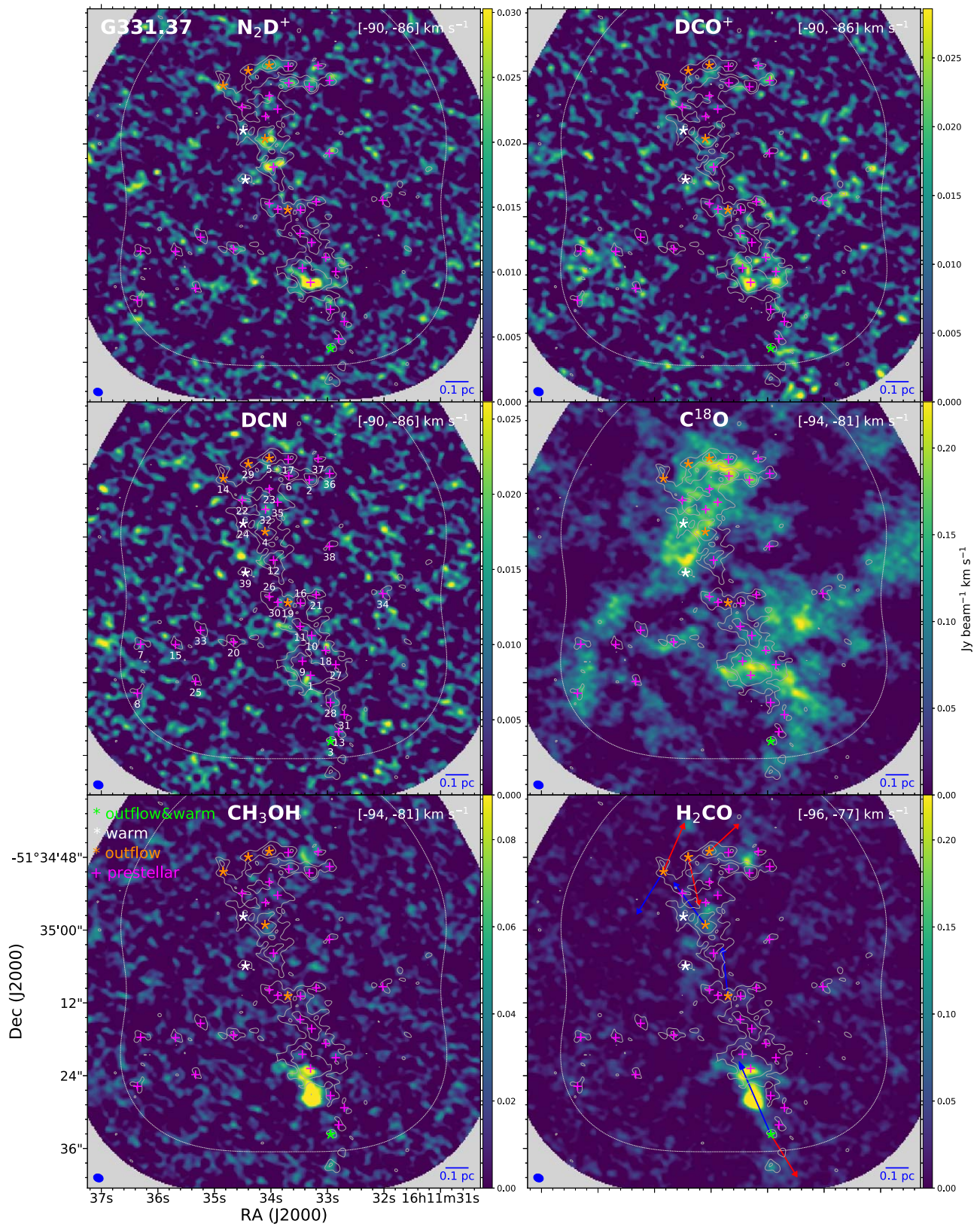**Figure 10.** (Continued.)

Figure 10. (Continued.)

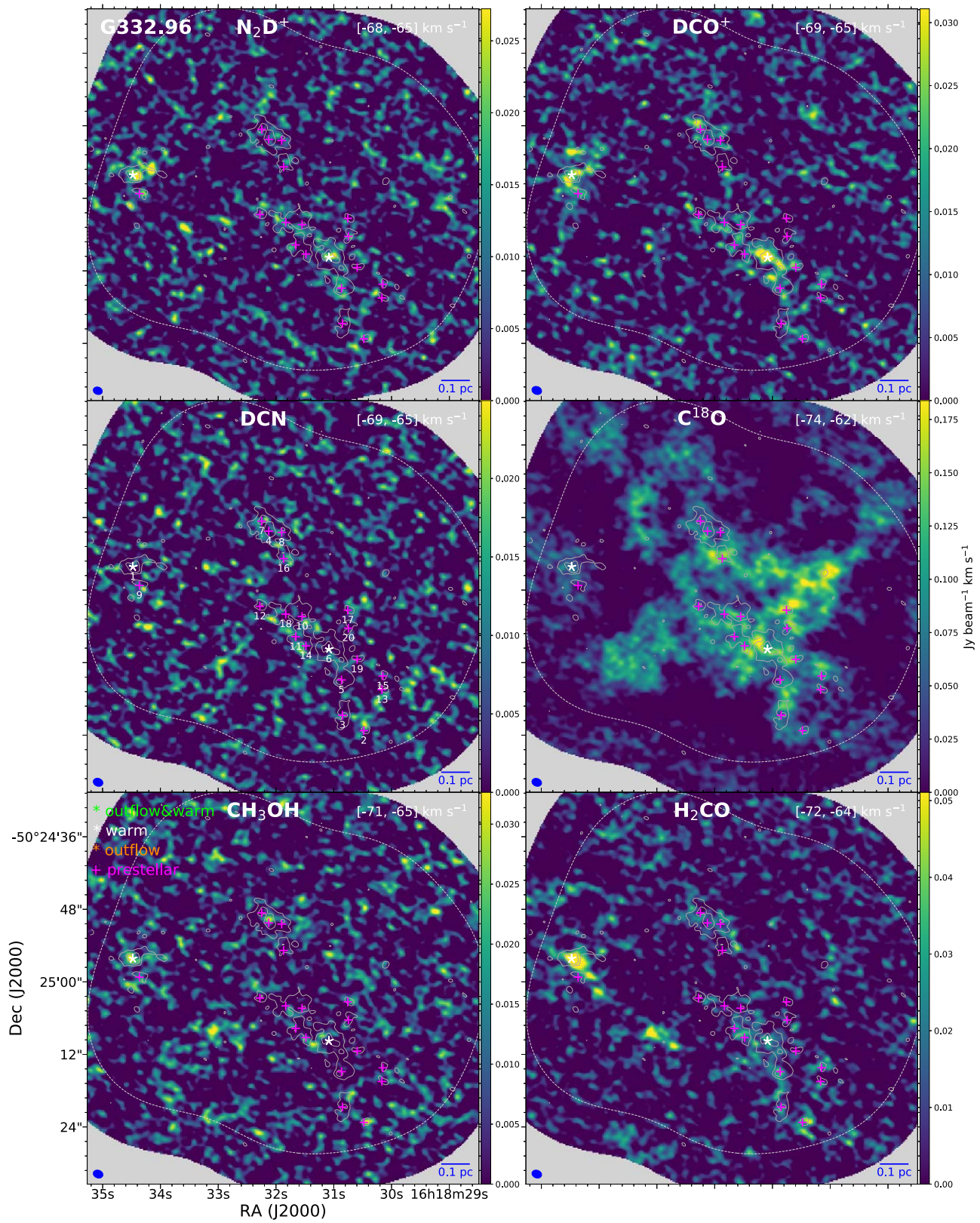**Figure 11.** The same as Figure 10, but for different sources.
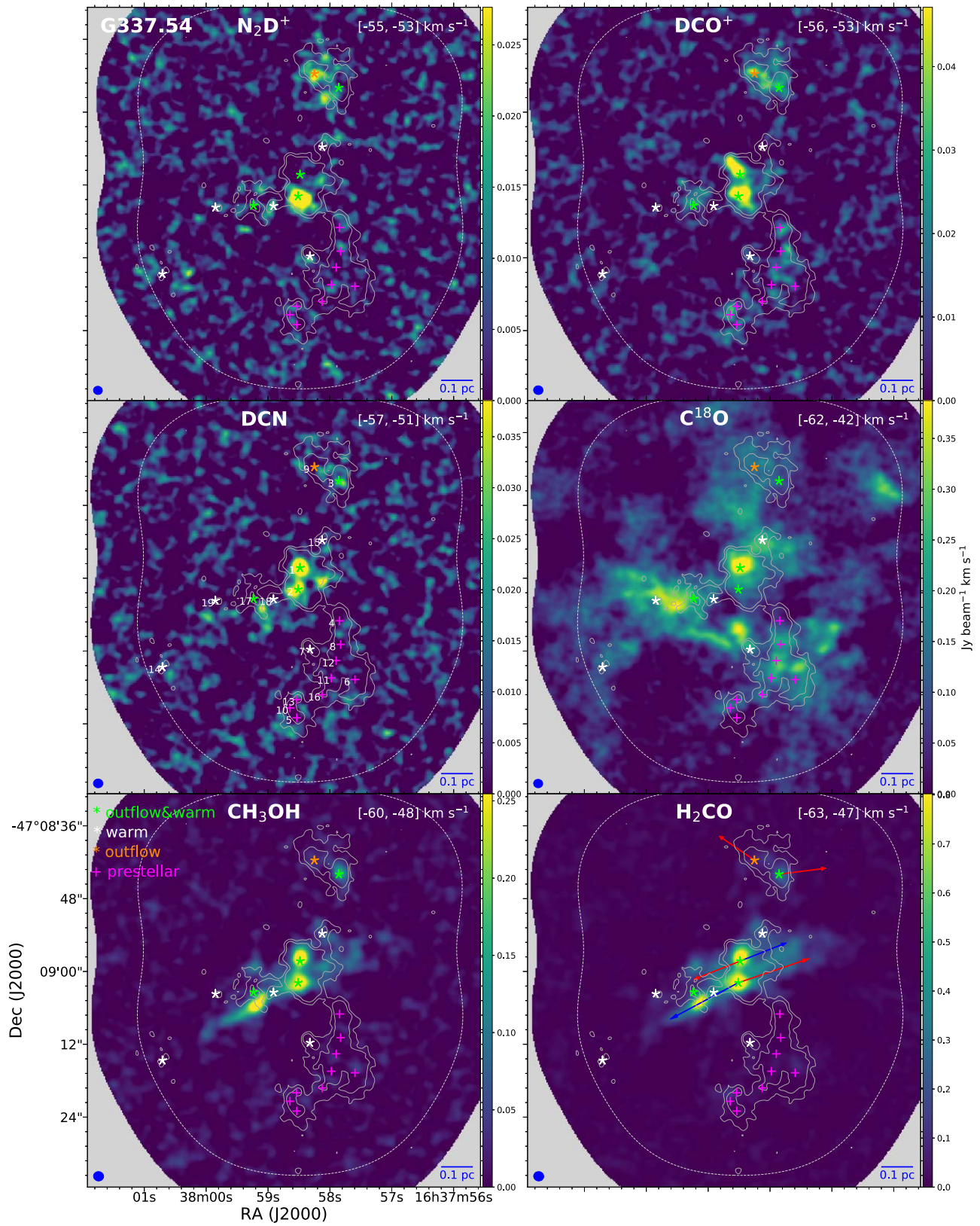
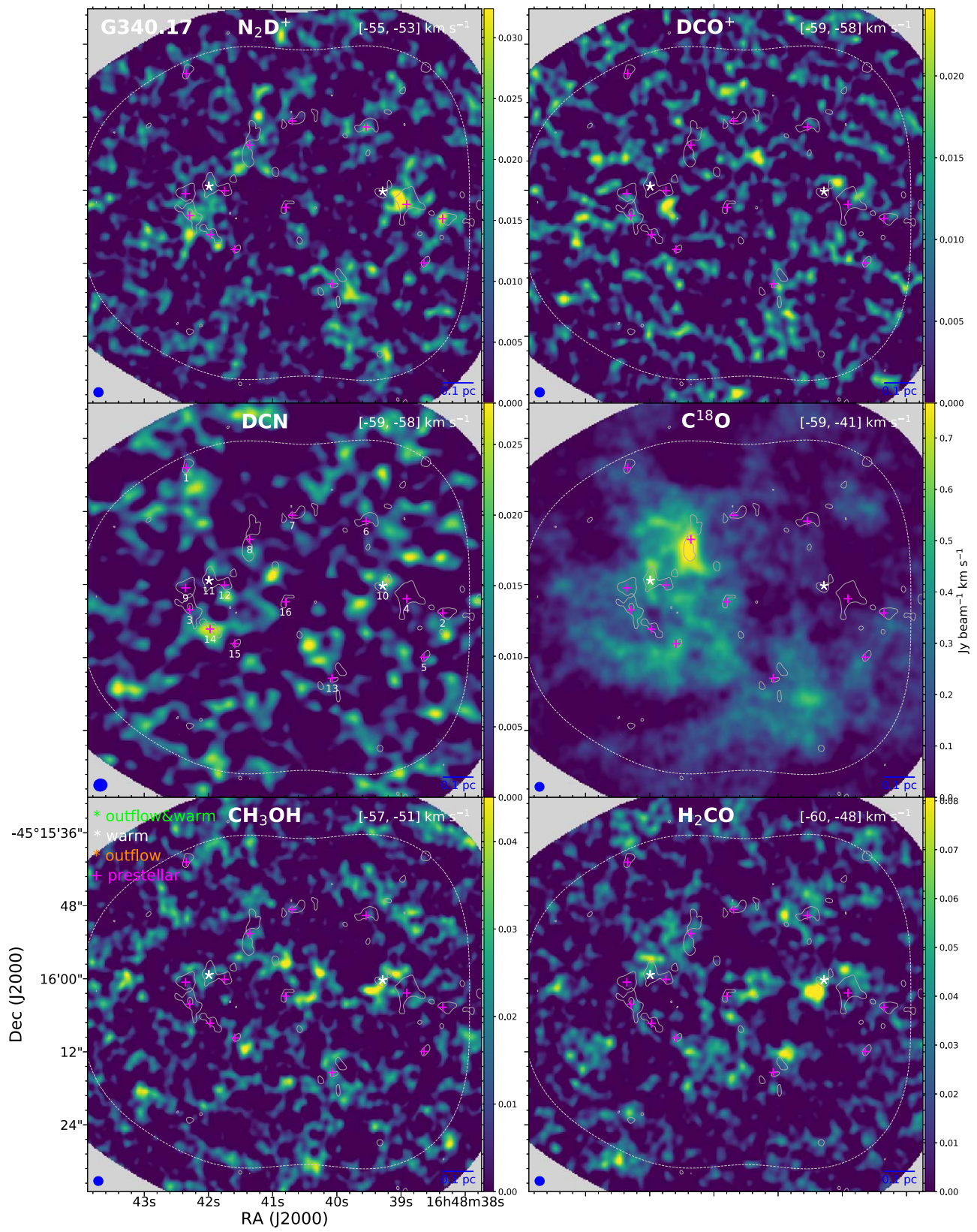**Figure 11.** (Continued.)

Figure 11. (Continued.)

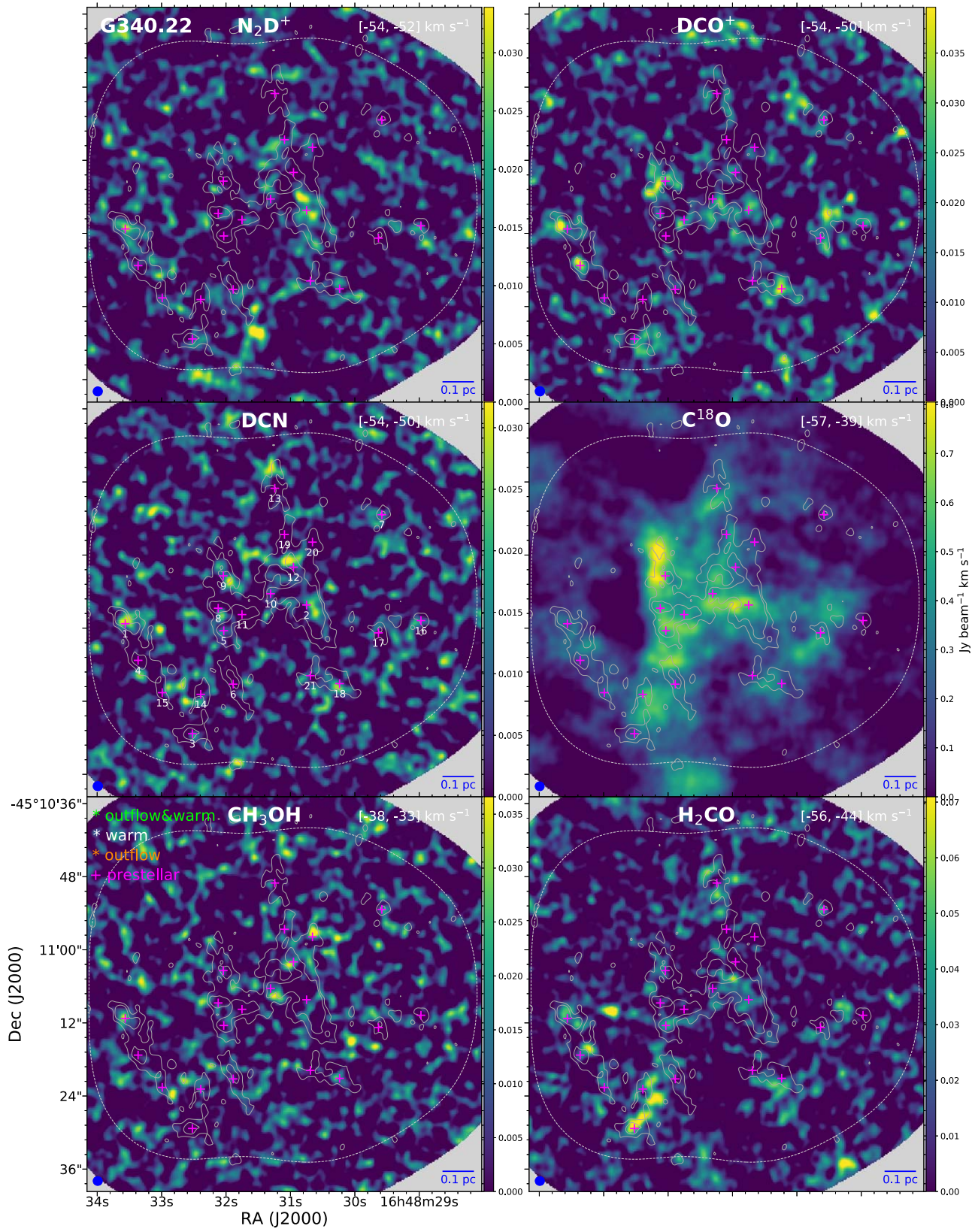**Figure 12.** The same as Figure 10, but for different sources.

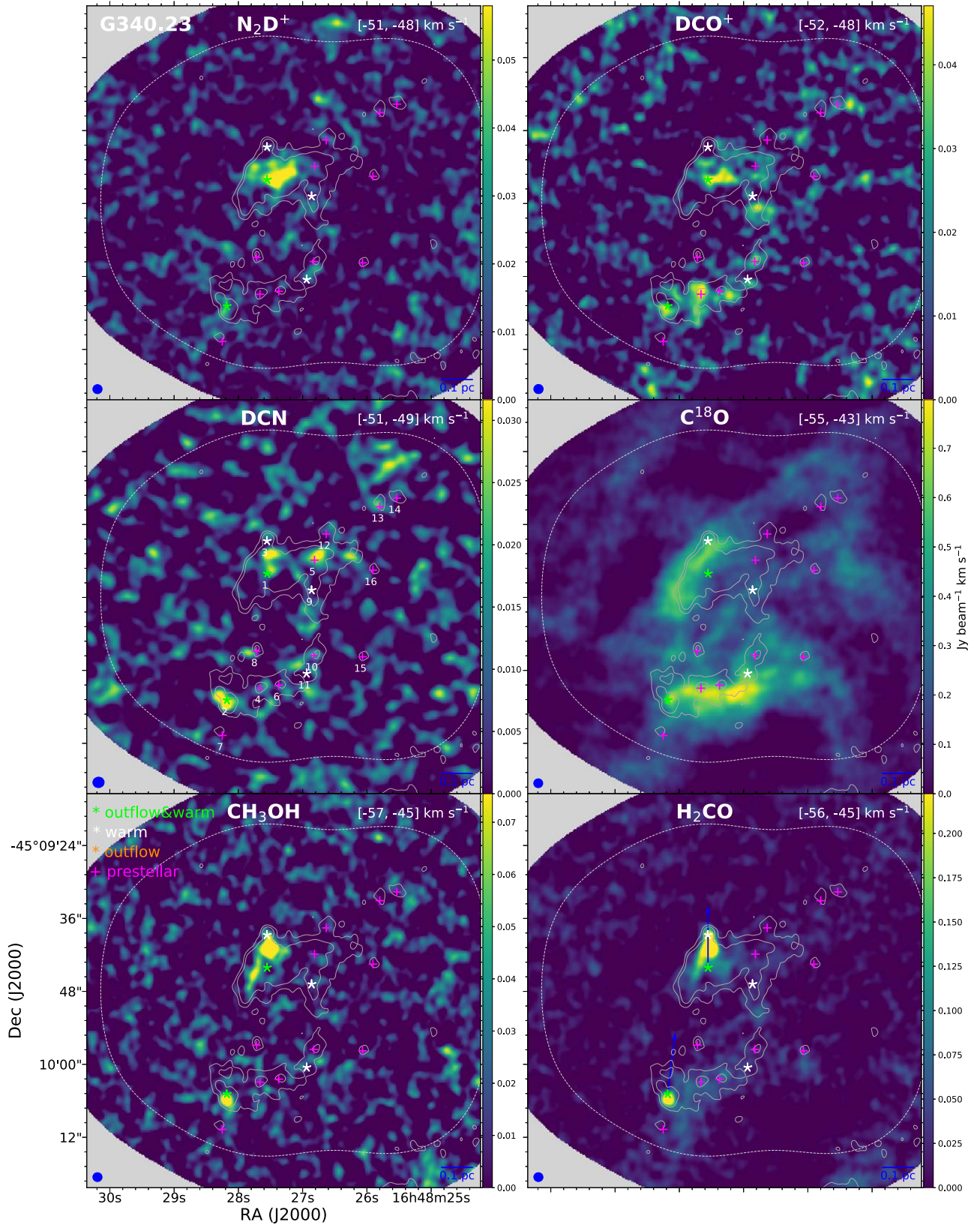**Figure 13.** The same as Figure 10, but for different sources.
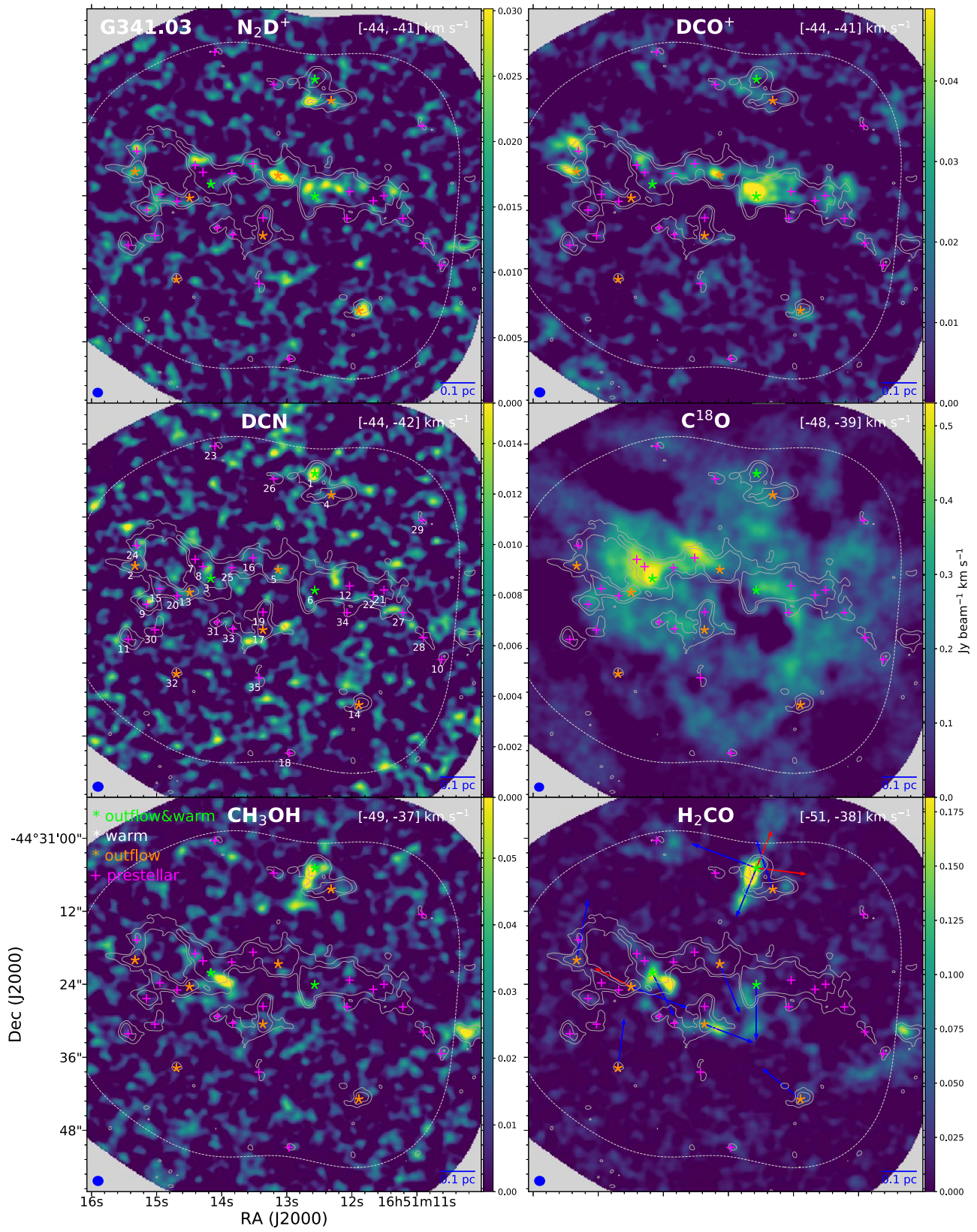
Figure 13. (Continued.)
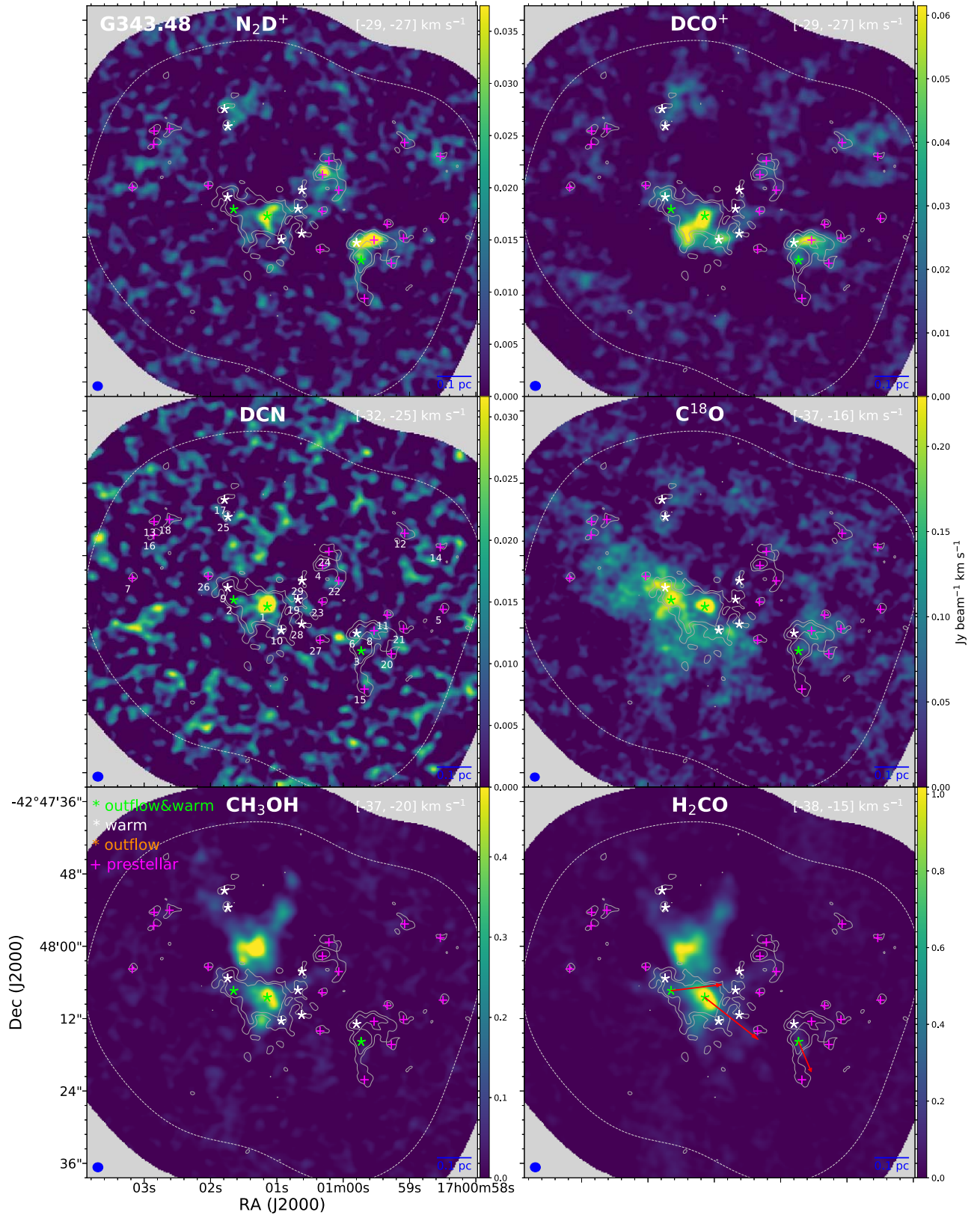
Figure 13. (Continued.)

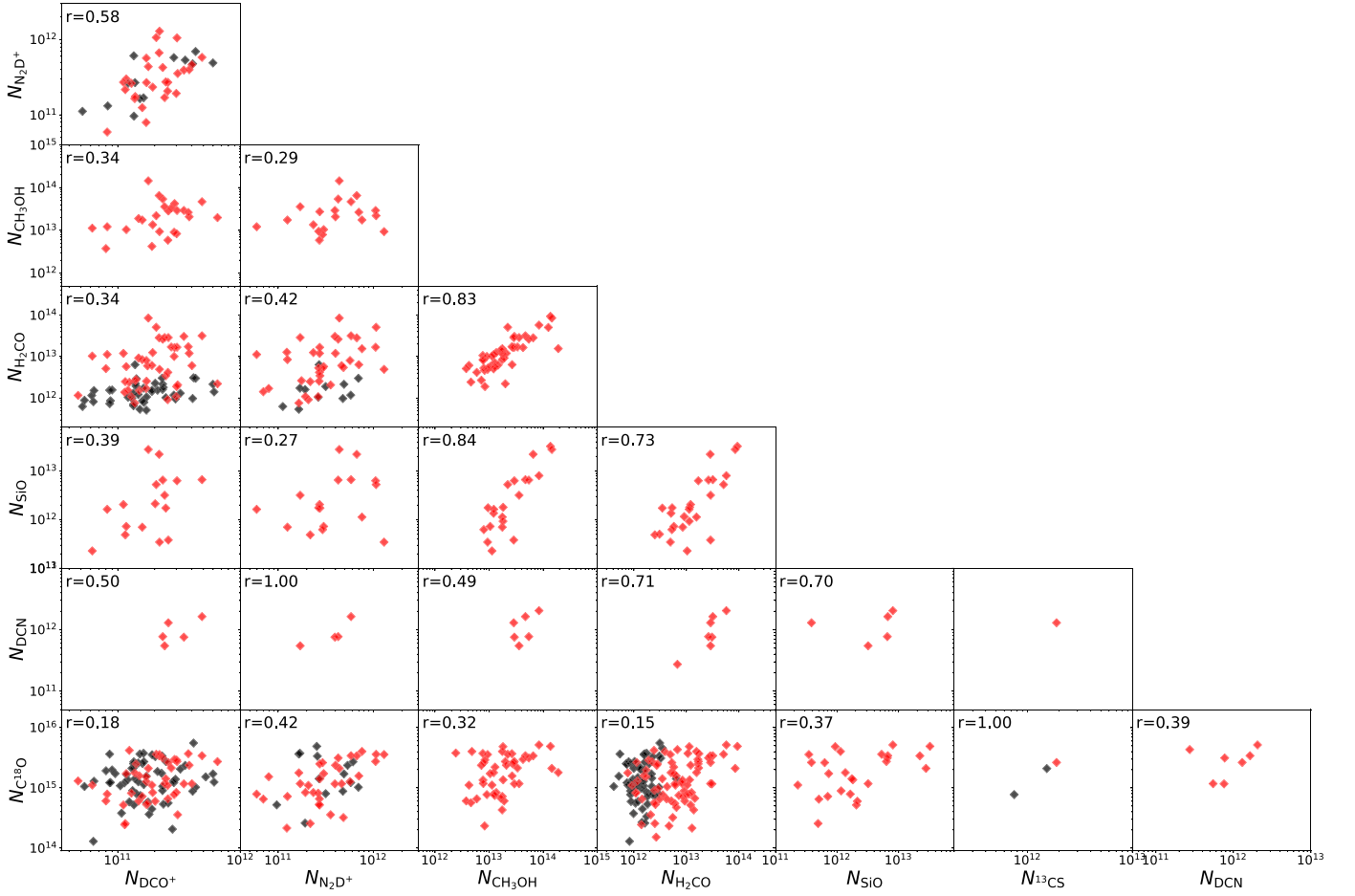**Figure 14.** The same as Figure 10, but for different sources.

Figure 15. The column densities of each molecule plotted against each other. The black and red points represent the prestellar and protostellar cores, respectively.

Table 5
Summary of the Derived Parameters of Detected Lines

Molecule	Core	N_{H_2} $\times 10^{22}$ cm^{-2}	n_{H_2} $\times 10^5$ cm^{-3}	T_{NH_3} K	$I_{C^{18}O}$ K	$v_{C^{18}O}$ km s^{-1}	$\sigma_{C^{18}O}$ km s^{-1}	$N_{C^{18}O}$ $\times 10^{14}$ cm^{-2}	I_{DCO^+} K	v_{DCO^+} km s^{-1}	...
G10.99	1	4.78	1.59	13.4	0.69 (0.09)	0.69 (0.09)	30.16 (0.12)	0.76 (0.12)	0.41 (0.03)	29.75 (0.03)	...
G10.99	2	8.31	7.80	12.5	0.39 (0.08)	0.39 (0.08)	29.96 (0.13)	0.49 (0.11)	...	...	...
G10.99	3	7.80	5.21	11.7	0.65 (0.04)	0.65 (0.04)	29.92 (0.07)	1.07 (0.07)	0.51 (0.05)	29.63 (0.05)	...
G10.99	4	4.41	2.80	13.0	...	...	...	...	...	...	...
G10.99	5	5.55	2.33	13.3	0.62 (0.04)	0.62 (0.04)	29.28 (0.09)	1.12 (0.09)	0.79 (0.11)	29.90 (0.03)	...
G10.99	6	5.55	5.51	13.0	...	...	...	...	...	...	...
G10.99	7	5.29	2.15	12.3	1.23 (0.05)	1.23 (0.05)	29.62 (0.04)	0.85 (0.04)	1.74 (0.07)	29.56 (0.01)	...
G10.99	8	4.92	1.59	12.2	0.80 (0.04)	0.80 (0.04)	30.13 (0.04)	0.70 (0.04)	0.44 (0.06)	29.83 (0.05)	...
G10.99	9	4.25	2.43	13.3	0.84 (0.05)	0.84 (0.05)	29.38 (0.05)	0.74 (0.05)	0.66 (0.07)	29.52 (0.04)	...
G10.99	10	3.32	1.53	11.7	...	...	...	...	0.29 (0.05)	30.46 (0.05)	...
G10.99	11	5.56	6.16	11.4	0.33 (0.06)	0.33 (0.06)	30.74 (0.23)	1.10 (0.23)	0.87 (0.16)	29.78 (0.03)	...
G10.99	12	4.85	4.61	11.3	0.53 (0.09)	0.53 (0.09)	30.14 (0.11)	0.54 (0.11)	...	...	...
G10.99	13	3.21	1.55	13.0	0.80 (0.06)	0.80 (0.06)	28.99 (0.08)	0.96 (0.08)	...	...	...
G10.99	14	3.29	2.22	13.3	0.63 (0.07)	0.63 (0.07)	29.50 (0.13)	1.03 (0.13)	0.32 (0.06)	28.76 (0.08)	...
G10.99	15	3.38	1.66	13.3	1.10 (0.09)	1.10 (0.09)	29.54 (0.08)	0.91 (0.08)	...	...	...
...	...	...	...	...	...	...	...	...	...	...	...
G343.48	23	1.06	1.35	12.9	...	...	...	...	0.38 (0.06)	−28.62 (0.02)	...
G343.48	24	1.10	0.44	13.6	...	...	...	...	0.23 (0.04)	−28.93 (0.04)	...
G343.48	25	0.84	0.47	15.2	0.18 (0.02)	−28.25 (0.15)	0.92 (0.15)	2.32 (0.51)	...	...	...
G343.48	26	0.97	1.10	13.6	1.00 (0.03)	−28.84 (0.02)	0.60 (0.02)	8.78 (0.62)	...	...	...
G343.48	27	0.73	0.58	16.3	0.46 (0.03)	−28.73 (0.04)	0.40 (0.02)	2.63 (0.25)	...	...	...
G343.48	28	0.77	0.61	16.4	0.81 (0.03)	−28.40 (0.02)	0.52 (0.02)	6.05 (0.47)	0.33 (0.05)	−28.38 (0.03)	...
G343.48	29	1.05	0.62	12.0	0.11 (0.02)	−26.20 (0.17)	0.88 (0.17)	1.52 (0.40)	...	...	...

Note. This table contains the column density, volume density, T_{NH_3}, and the derived parameters of the lines for each dense core.

(This table is available in its entirety in machine-readable form.)

densities. Table 5 summarizes the derived parameters of the detected lines.

Appendix B
Ammonia Excitation Temperature

The excitation temperatures were obtained using the method described in Mangum & Shirley (2015). The ammonia (1,1) and (2,2) transition spectra were modeled using five-component Gaussian models with seven parameters (systemic velocity, line width, and five amplitude parameters, one for each hyperfine component). The best-fit model parameters were obtained using scipy's "curve_fit" routine, using the TRF ("Trust Region Reflective") algorithm.

From these parameters, the optical depth for the (1,1) transition, $\tau(1, 1)$, was calculated from the ratio of the brightness of the satellite hyperfine transitions to the main component; this was solved numerically, using scipy's "root" routine, using the Levenberg–Marquardt algorithm to minimize the sum of squared errors of the four ratios simultaneously.

Finally, the brightness temperatures, $T_B(1, 1)$ and $T_B(2, 2)$, and the optical depth were combined with the line width parameter ($\Delta v(1, 1)$ and $\Delta v(2, 2)$, common to all hyperfine components) to calculate the excitation temperature, T_{NH_3}, as

$$T_{NH_3} = \frac{-41.5}{\ln\left[-\frac{0.283\Delta v(2,2)}{\tau(1,1)\Delta v(1,1)}\ln\left(1 - \frac{T_B(2,2)}{T_B(1,1)}(1 - \exp[-\tau(1, 1)])\right)\right]}. \quad (B1)$$

The full details of this method for calculating the optical depth and excitation temperature are given in Mangum & Shirley (2015).

The error bounds for the excitation temperature were then computed using a Monte Carlo approach. For each model parameter, a randomized value was repeatedly drawn (1000 times) from a Gaussian distribution, with the mean equal to the optimal parameter value and the variance equal to the variance of the parameter estimates, as reported by the fitting routine. The optical depth and excitation temperature were then calculated using each set of randomized parameters, and the variance of the resulting distribution was calculated to yield the temperature uncertainty.

Appendix C
Column Density

Assuming LTE and thin optical depths in the molecular line, the column densities of the molecules can be calculated following Mangum & Shirley (2015):[18]

$$N_{mol} = \frac{3h}{8\pi^3R} \frac{Q_{rot}}{S\mu^2 g_u} \frac{\exp(E_u/kT_{ex})}{\exp(h\nu/kT_{ex}) - 1}$$
$$\times (J_\nu(T_{ex}) - J_\nu(T_{bg}))^{-1} \int \frac{T_B dv}{f}, \quad (C1)$$

where h is the Planck constant, $S\mu^2$ is the line strength multiplied by the square of the dipole moment, R is the relative intensity of the main hyperfine transition with respect to the rest of the hyperfine transitions, g_u is the statistical weight of the upper level, T_{ex} is the excitation temperature, T_{bg} is the background temperature, E_u is the energy of the upper state, ν

is the transition frequency, T_B is the brightness temperature, $\int T_B dv$ is the velocity-integrated intensity, f is the filling factor, and Q_{rot} is the partition function. Here, f is assumed to be 1 and T_{NH_3} approximates the T_{ex} of the molecular lines.

The molecular column density N_{H_2}, gas mass M_{gas}, and volume density n_{H_2} are derived from the continuum emission, with

$$N_{H_2} = \eta \frac{S_\nu}{B_\nu(T)\,\kappa_\nu\,\Omega\,\mu m_H}, \quad (C2)$$

$$M_{gas} = \eta \frac{F_\nu\,D^2}{\kappa_\nu\,B_\nu(T)}, \quad (C3)$$

$$n_{H_2} = \frac{M_{gas}}{\frac{4}{3}\pi r^3\,\mu m_H}, \quad (C4)$$

where $\eta = 100$ is the gas-to-dust ratio, S_ν is the peak flux density, F_ν is the measured integrated source flux, Ω is the beam solid angle, m_H is the mass of a hydrogen atom, $\mu = 2.8$ is the mean molecular weight of the interstellar medium (Kauffmann et al. 2008), κ_ν is the dust opacity at a frequency of ν, D is the distance to the source, and r is the radius of the dense core. We adopted a value of 0.9 cm^{-2} g^{-1} for $\kappa_{1.3mm}$, which corresponds to the opacity of thin ice mantles, and a gas density of 10^6 cm^{-3} (Ossenkopf & Henning 1994).

The flux density is converted to the brightness temperature following[19]

$$T_B = 1.222 \times 10^3 \frac{I}{\nu^2\,\theta_{maj}\,\theta_{min}}, \quad (C5)$$

where T_B is the brightness temperature in K, I is the flux in mJy beam^{-1}, ν is the frequency in GHz, and θ_{maj} and θ_{min} are the half-power beam widths along the major and minor axes, respectively.

ORCID iDs

Shanghuo Li ● https://orcid.org/0000-0003-1275-5251
Patricio Sanhueza ● https://orcid.org/0000-0002-7125-7685
Xing Lu ● https://orcid.org/0000-0003-2619-9305
Chang Won Lee ● https://orcid.org/0000-0002-3179-6334
Qizhou Zhang ● https://orcid.org/0000-0003-2384-6589
Stefano Bovino ● https://orcid.org/0000-0003-2814-6688
Giovanni Sabatini ● https://orcid.org/0000-0002-6428-9806
Tie Liu ● https://orcid.org/0000-0002-5286-2564
Kee-Tae Kim ● https://orcid.org/0000-0003-2412-7092
Kaho Morii ● https://orcid.org/0000-0002-6752-6061
Daniel Tafoya ● https://orcid.org/0000-0002-2149-2660
Ken'ichi Tatematsu ● https://orcid.org/0000-0002-8149-8546
Takeshi Sakai ● https://orcid.org/0000-0003-4521-7492
Junzhi Wang ● https://orcid.org/0000-0001-6106-1171
Fei Li ● https://orcid.org/0000-0002-9832-8295
Andrea Silva ● https://orcid.org/0000-0001-9500-604X
Natsuko Izumi ● https://orcid.org/0000-0003-1604-9127
David Allingham ● https://orcid.org/0000-0002-4173-2852

References

Albertsson, T., Semenov, D. A., Vasyunin, A. I., Henning, T., & Herbst, E. 2013, ApJS, 207, 27

---

[18] https://github.com/ShanghuoLi/calcu

[19] https://science.nrao.edu/facilities/vla/proposing/TBconv

Arce, H. G., Santiago-García, J., Jørgensen, J. K., Tafalla, M., & Bachiller, R. 2008, ApJL, 681, L21

Astropy Collaboration, Robitaille, T. P., Tollerud, E. J., et al. 2013, A&A, 558, A33

Barnes, A. T., Kong, S., Tan, J. C., et al. 2016, MNRAS, 458, 1990

Bergin, E. A., & Tafalla, M. 2007, ARA&A, 45, 339

Bernstein, M. P., Dworkin, J. P., Sandford, S. A., Cooper, G. W., & Allamandola, L. J. 2002, Natur, 416, 401

Bisschop, S. E., Jørgensen, J. K., van Dishoeck, E. F., & de Wachter, E. B. M. 2007, A&A, 465, 913

Booth, A. S., Walsh, C., Terwisscha van Scheltinga, J., et al. 2021, NatAs, 5, 684

Caselli, P., & Ceccarelli, C. 2012, A&ARv, 20, 56

Caselli, P., Walmsley, C. M., Zucconi, A., et al. 2002, ApJ, 565, 344

Charnley, S. B., Tielens, A. G. G. M., & Rodgers, S. D. 1997, ApJL, 482, L203

Chen, H.-R., Liu, S.-Y., Su, Y.-N., & Zhang, Q. 2010, ApJL, 713, L50

Cohen, J. 1988, 1988 Statistical Power Analysis for the Behavioral Sciences (Hillsdale, NJ: L. Erlbaum Associates)

Contreras, Y., Sanhueza, P., Jackson, J. M., et al. 2018, ApJ, 861, 14

Dalgarno, A., & Lepp, S. 1984, ApJL, 287, L47

Drozdovskaya, M. N., van Dishoeck, E. F., Rubin, M., Jørgensen, J. K., & Altwegg, K. 2019, MNRAS, 490, 50

Feng, S., Li, D., Caselli, P., et al. 2020, ApJ, 901, 145

Fuchs, G. W., Cuppen, H. M., Ioppolo, S., et al. 2009, A&A, 505, 629

Garrod, R., Park, I. H., Caselli, P., & Herbst, E. 2006, FaDi, 133, 51

Garrod, R. T., Widicus Weaver, S. L., & Herbst, E. 2008, ApJ, 682, 283

Gerner, T., Beuther, H., Semenov, D., et al. 2014, A&A, 563, A97

Gerner, T., Shirley, Y. L., Beuther, H., et al. 2015, A&A, 579, A80

Giannetti, A., Bovino, S., Caselli, P., et al. 2019, A&A, 621, L7

Ginsburg, A., Sokolov, V., de Val-Borro, M., et al. 2022, AJ, 163, 291

Guzmán, A. E., Guzmán, V. V., Garay, G., Bronfman, L., & Hechenleitner, F. 2018, ApJS, 236, 45

Guzmán, V. V., Goicoechea, J. R., Pety, J., et al. 2013, A&A, 560, A73

Herbst, E., & van Dishoeck, E. F. 2009, ARA&A, 47, 427

Hoq, S., Jackson, J. M., Foster, J. B., et al. 2013, ApJ, 777, 157

Hunter, J. D. 2007, CSE, 9, 90

Immer, K., Galván-Madrid, R., König, C., Liu, H. B., & Menten, K. M. 2014, A&A, 572, A63

Jørgensen, J. K., Belloche, A., & Garrod, R. T. 2020, ARA&A, 58, 727

Jørgensen, J. K., Schöier, F. L., & van Dishoeck, E. F. 2005, A&A, 437, 501

Kauffmann, J., Bertoldi, F., Bourke, T. L., Evans, N. J. I., & Lee, C. W. 2008, A&A, 487, 993

Kong, S., Tan, J. C., Caselli, P., et al. 2017, ApJ, 834, 193

Le Teuff, Y. H., Millar, T. J., & Markwick, A. J. 2000, A&AS, 146, 157

Leurini, S., Parise, B., Schilke, P., Pety, J., & Rolffs, R. 2010, A&A, 511, A82

Li, S., Lu, X., Zhang, Q., et al. 2021, ApJL, 912, L7

Li, S., Sanhueza, P., Zhang, Q., et al. 2020, ApJ, 903, 119

Li, S., Wang, J., Fang, M., et al. 2019, ApJ, 878, 29

Li, S., Wang, J., Zhang, Z.-Y., et al. 2017, MNRAS, 466, 248

Liu, H.-L., Sanhueza, P., Liu, T., et al. 2020, ApJ, 901, 31

Lu, X., Li, S., Ginsburg, A., et al. 2021, ApJ, 909, 177

Mangum, J. G., & Shirley, Y. L. 2015, PASP, 127, 266

Maret, S., Ceccarelli, C., Caux, E., et al. 2004, A&A, 416, 577

Maret, S., Ceccarelli, C., Tielens, A. G. G. M., et al. 2005, A&A, 442, 527

McMullin, J. P., Waters, B., Schiebel, D., Young, W., & Golap, K. 2007, in ASP Conf. Ser., 376, Astronomical Data Analysis Software and Systems XVI, ed. R. A. Shaw, F. Hill, & D. J. Bell (San Francisco, CA: ASP), 127

Miettinen, O. 2014, A&A, 562, A3

Morii, K., Sanhueza, P., Nakamura, F., et al. 2021, ApJ, 923, 147

Mottram, J. C., Beuther, H., Ahmadi, A., et al. 2020, A&A, 636, A118

Muñoz Caro, G. M., Meierhenrich, U. J., Schutte, W. A., et al. 2002, Natur, 416, 403

Müller, H. S. P., Schlöder, F., Stutzki, J., & Winnewisser, G. 2005, JMoSt, 742, 215

Öberg, K. I., & Bergin, E. A. 2021, PhR, 893, 1

Ossenkopf, V., & Henning, T. 1994, A&A, 291, 943

Pagani, L., Bacmann, A., Cabrit, S., & Vastel, C. 2007, A&A, 467, 179

Pagani, L., Vastel, C., Hugo, E., et al. 2009, A&A, 494, 623

Peng, Y., Liu, T., Qin, S.-L., et al. 2022, MNRAS, 512, 4419

Pineda, J. E., Harju, J., Caselli, P., et al. 2022, AJ, 163, 294

Qin, S.-L., Liu, T., Liu, X., et al. 2022, MNRAS, 511, 3463

Redaelli, E., Bizzocchi, L., Caselli, P., et al. 2019, A&A, 629, A15

Redaelli, E., Bovino, S., Giannetti, A., et al. 2021, A&A, 650, A202

Requena-Torres, M. A., Martín-Pintado, J., Rodríguez-Franco, A., et al. 2006, A&A, 455, 971

Robitaille, T., & Bressert, E. 2012, APLpy: Astronomical Plotting Library in Python, Astrophysics Source Code Library, ascl:1208.017

Rosolowsky, E. W., Pineda, J. E., Kauffmann, J., & Goodman, A. A. 2008, ApJ, 679, 1338

Sabatini, G., Bovino, S., Giannetti, A., et al. 2020, A&A, 644, A34

Sabatini, G., Bovino, S., Giannetti, A., et al. 2021, A&A, 652, A71

Sabatini, G., Bovino, S., Sanhueza, P., et al. 2022, ApJ, 936, 80

Sabatini, G., Giannetti, A., Bovino, S., et al. 2019, MNRAS, 490, 4489

Sakai, N., Ceccarelli, C., Bottinelli, S., Sakai, T., & Yamamoto, S. 2012, ApJ, 754, 70

Sakai, T., Sanhueza, P., Furuya, K., et al. 2022, ApJ, 925, 144

Sanhueza, P., Contreras, Y., Wu, B., et al. 2019, ApJ, 886, 102

Sanhueza, P., Garay, G., Bronfman, L., et al. 2010, ApJ, 715, 18

Sanhueza, P., Jackson, J. M., Foster, J. B., et al. 2012, ApJ, 756, 60

Sanhueza, P., Jackson, J. M., Foster, J. B., et al. 2013, ApJ, 773, 123

Sanhueza, P., Jackson, J. M., Zhang, Q., et al. 2017, ApJ, 841, 97

Schöier, F. L., van der Tak, F. F. S., van Dishoeck, E. F., & Black, J. H. 2005, A&A, 432, 369

Tafalla, M., Santiago-García, J., Hacar, A., & Bachiller, R. 2010, A&A, 522, A91

Tafalla, M., Santiago-García, J., Myers, P. C., et al. 2006, A&A, 455, 577

Tafoya, D., Sanhueza, P., Zhang, Q., et al. 2021, ApJ, 913, 131

Turner, B. E. 2001, ApJS, 136, 579

Tychoniec, Ł., van Dishoeck, E. F., van 't Hoff, M. L. R., et al. 2021, A&A, 655, A65

van Dishoeck, E. F., & Blake, G. A. 1998, ARA&A, 36, 317

Vasyunina, T., Vasyunin, A. I., Herbst, E., et al. 2014, ApJ, 780, 85

Watanabe, N., Nagaoka, A., Shiraki, T., & Kouchi, A. 2004, ApJ, 616, 638

Wootten, A., & Loren, R. B. 1987, ApJ, 317, 220